Faddeev calculations of muonic-atom collisions: Scattering and fusion in flight

Andrei A. Kvitsinsky* and Chi-Yu Hu
Department of Physics, California State University, Long Beach, California 90840

James S. Cohen
Theoretical Division, Los Alamos National Laboratory, Los Alamos, New Mexico 87545
(Received 11 April 1995; revised manuscript received 28 August 1995)

The Faddeev approach is used to study s-wave scattering and fusion in flight for the muonic-atomic systems $p+p\mu$, $d+d\mu$, $t+t\mu$, $d+t\mu$, and $t+d\mu$ in a broad energy range below the $n=2$ threshold of the target muonic atom. Clear manifestations of near-threshold virtual states in the $p+p\mu$ and $t+t\mu$ systems are seen, e.g., in large amplifications of the fusion-in-flight reaction rates near zero energy. Peaks and minima (essentially exact zeros for the symmetric systems) in the fusion-in-flight rates are also seen at finite energies. In the case of $d+t\mu$, the fusion-in-flight rate (at liquid-hydrogen density) reaches a value of 3.40×10^{6} s^{-1} for collisions at 76.3 eV, which may be compared with the rate 1.14×10^{5} s^{-1} at thermal energies.

PACS number(s): 11.80.Jy, 36.10.Dr, 25.30.Mr, 34.70.+e

I. INTRODUCTION

This paper deals with the s-wave scattering in the symmetric muonic-atomic systems

$$a+a\mu(n=1), a=p,d,\text{or } t, \tag{1}$$

and in the asymmetric system

$$d+t\mu(n=1), \quad t+d\mu(n=1). \tag{2}$$

Much interest in the muonic-atom collisions is due to the roles they play in the muon-catalyzed-fusion cycles [1–3]. Also, theoretical interest stems from the facts that muonic systems (i) bridge the huge energy gap between the nuclear and atomic domains and (ii) interpolate between two kinematic limits of a three-body Coulomb system: atomic systems such as $e^{-}+\mathrm{H}$, consisting of one heavy and two light particles, and molecular systems such as H_2^{+}, involving one light and two heavy particles.

Most previous scattering calculations for muonic atoms have been done via the Born-Oppenheimer adiabatic representation [4–8], which for normal atoms often allows one to treat essentials by taking into account only a few adiabatic channels. However, for collisions of muonic atoms sometimes hundreds of adiabatic basis functions are needed in order to achieve accuracies of a few percent [5,6].

In this paper we exploit a completely different approach to muonic-atom scattering problems. It is based on the modified Faddeev equations [9] in the total-angular-momentum representation [10]. This approach has been developed recently [11] and turns out to be a very powerful tool for solving three-body Coulomb scattering problems. A key feature is that it provides a simple and natural way to incorporate proper asymptotic conditions for scattering wave functions. The numerical solution is obtained directly by making use of an overall spline expansion of the Faddeev components in all variables. Convergence of the spline expansion is straightforward to achieve and its accuracy is easy to control.

The method does not involve any intermediate approximations; thus it may lack some qualitative insight lent by the adiabatic approximation. But from a computational point of view, this actually can be regarded as an advantage, for the method can be applied with equal ease to the systems amenable to the adiabatic expansion method (such as $d+t\mu$) as well as to those beyond it (such as $e^{\pm}+\mathrm{H}$ [12]). Thus the Faddeev approach allows one to treat uniformly a broad variety of Coulomb systems that otherwise have to be studied using quite different techniques (variational, adiabatic, coupled channels, etc.). Application of the Faddeev approach to the muonic-atomic systems is another important illustration of this fact.

Most calculations of muonic atom scattering have been done in the context of muon-catalyzed fusion, where collision energies up to a few eV are of main concern. At such low energies, purely three-body aspects of the problem are somewhat shadowed by effects due to the hyperfine interaction between nuclei and muon (especially in the $p+p\mu$ scattering). In the present work, we treat scattering up to 1 keV. That is too high to be of practical importance for muon-catalyzed fusion; however, accurate description of the muonic-atomic collisions is of general interest for few-body physics and can also be used in other aspects of muon physics. The Faddeev approach provides an effective tool for the entire energy range.

Besides usual cross section calculations, we also study the fusion-in-flight reactions in the muonic-atomic systems (1) and (2). At low energies the description of such reactions by a simple tunneling factor is essentially irrelevant.

II. FADDEEV EQUATIONS

Our approach is based on the Faddeev decomposition of the wave function into three components related to the three kinematic channels of a three-body system. The Faddeev method [13], originally developed for short-range interac-

*Permanent address: Department of Mathematical and Computational Physics, Institute for Physics, University of St. Petersburg, St. Petersburg 198904, Russia.

tions [14], was later modified by Merkuriev [9] in order to incorporate long-range Coulomb potentials. The resulting modified Faddeev equations are, of course, equivalent to the underlying Schrödinger equation but facilitate setting up the asymptotic boundary conditions for scattering problems. The reason is that each Faddeev component is described in terms of its own set of Jacobi vectors, related to the corresponding asymptotic channel, while in the Schrödinger wave function all the channels are mixed up.

To describe the Faddeev equations, we first introduce some standard notations [9–11]. Labels $\alpha=1,2,3$ index the particles of the muonic-atomic systems, with $\alpha=3$ being the index of the muon. Also, α labels pairs of particles with members $\beta\neq\alpha$ (e.g., pair 1 consists of particles 2 and 3) and the corresponding asymptotic channels. For $(dt\mu)=(123)$, then channels 1 and 2 are $d+t\mu$ and $t+d\mu$, respectively. We make use of muonic-atomic units (m.a.u.), $\hbar=e=m_\mu=1$, so that the unit of length is the muonic Bohr radius $a_\mu=\hbar^2/e^2m_\mu=2.56\times10^{-11}$ cm.

Three-body kinematics in each channel α is most conveniently described using the corresponding set of the mass-scaled Jacobi vectors $\{\mathbf{x}_\alpha,\mathbf{y}_\alpha\}$ defined by

$$\mathbf{x}_\alpha=\tau_\alpha(\mathbf{r}_\beta-\mathbf{r}_\gamma) \tag{3a}$$

and

$$\mathbf{y}_\alpha=\mu_\alpha\left(\mathbf{r}_\alpha-\frac{m_\beta\mathbf{r}_\beta+m_\gamma\mathbf{r}_\gamma}{m_\beta+m_\gamma}\right), \tag{3b}$$

where $(\alpha\beta\gamma)=$ cyclic (123), m_α and $\mathbf{r}_\alpha$ are the particle masses and position vectors,

$$\tau_\alpha=\sqrt{2\frac{m_\beta m_\gamma}{m_\beta+m_\gamma}}, \tag{4a}$$

$$\mu_\alpha=\sqrt{2m_\alpha\left(1-\frac{m_\alpha}{M}\right)}, \tag{4b}$$

and

$$M=m_1+m_2+m_3, \tag{4c}$$

so that $\tau_\alpha^2/2$ is the reduced mass of pair α and $\mu_\alpha^2/2$ is the reduced mass of the particle α and the pair α. The Jacobi vectors of different channels are related by orthogonal transformations

$$\mathbf{x}_\beta=c_{\beta\alpha}\mathbf{x}_\alpha+s_{\beta\alpha}\mathbf{y}_\alpha, \tag{5a}$$

$$\mathbf{y}_\beta=-s_{\beta\alpha}\mathbf{x}_\alpha+c_{\beta\alpha}\mathbf{y}_\alpha \tag{5b}$$

with the mass-dependent coefficients

$$c_{\beta\alpha}=-\left[\frac{m_\beta m_\alpha}{(M-m_\beta)(M-m_\alpha)}\right]^{1/2}, \tag{6a}$$

$$s_{\beta\alpha}=(-1)^{\beta-\alpha}\mathrm{sgn}(\alpha-\beta)(1-c_{\beta\alpha}^2)^{1/2}. \tag{6b}$$

Hereafter we shall only consider the state of total angular momentum zero (s wave). Then the three-body configuration space is a three-dimensional manifold (''internal space''), which can be parametrized by any three coordinates that fix the particle configuration in a plane. For scattering problems the most convenient choice for the local coordinates is the lengths of the Jacobi vectors and angle between them

$$x_\alpha=|\mathbf{x}_\alpha|, \tag{7a}$$

$$y_\alpha=|\mathbf{y}_\alpha|, \tag{7b}$$

$$\theta_\alpha=\arccos\left(\frac{(\mathbf{x}_\alpha,\mathbf{y}_\alpha)}{|\mathbf{x}_\alpha||\mathbf{y}_\alpha|}\right). \tag{7c}$$

The s-wave Hamiltonian is given by

$$H=H_0+\sum_{\alpha=1}^{3}V_\alpha(x_\alpha), \tag{8}$$

where V_α is the Coulomb potential for the pair $\alpha=(\beta,\gamma)$,

$$V_\alpha(x_\alpha)=\frac{q_\alpha}{x_\alpha}, \tag{9a}$$

$$q_\alpha=z_\beta z_\gamma\tau_\alpha, \tag{9b}$$

and z_β are particle charges; here q_α are the mass-scaled charges corresponding to Eq. (3). The kinetic-energy operator H_0 is a three-dimensional partial differential operator [10]

$$H_0=-x_\alpha^{-2}\partial_{x_\alpha}x_\alpha^2\partial_{x_\alpha}-y_\alpha^{-2}\partial_{y_\alpha}y_\alpha^2\partial_{y_\alpha}-[x_\alpha^{-2}+y_\alpha^{-2}]\csc\theta_\alpha\partial_{\theta_\alpha}\sin\theta_\alpha\partial_{\theta_\alpha}, \tag{10}$$

which is invariant in the channel index α. Table I gives all mass-dependent parameters related to the scaled Jacobi vectors (3) for the muonic-atomic systems (1) and (2).

TABLE I. Numerical values of the kinematic parameters (in m.a.u.) for Eqs. (3)–(9). The other six sets of the coefficients $\{c_{\alpha\beta},s_{\alpha\beta}\}$ are obtained by permutations: $c_{\beta\alpha}=c_{\alpha\beta}$, $s_{\beta\alpha}=-s_{\alpha\beta}$.

(123)	$(pp\mu)$	$(dd\mu)$	$(tt\mu)$	$(dt\mu)$
τ_1	1.3407	1.3760	1.3883	1.3883
τ_2	1.3407	1.3760	1.3883	1.3760
τ_3	2.9800	4.2133	5.1561	4.6139
μ_1	3.0584	4.2706	5.2034	4.6478
μ_2	3.0584	4.2706	5.2034	4.6895
μ_3	1.3760	1.3947	1.4011	1.3985
c_{12}	−0.8988	−0.9467	−0.9638	−0.9552
s_{12}	−0.4384	−0.3222	−0.2668	−0.2961
c_{13}	−0.2250	−0.1633	−0.1346	−0.1205
s_{13}	0.9744	0.9866	0.9909	0.9927
c_{23}	−0.2250	−0.1633	−0.1346	−0.1788
s_{23}	−0.9744	−0.9866	−0.9909	−0.9839
q_1	−1.3407	−1.3760	−1.3883	−1.3883
q_2	−1.3407	−1.3760	−1.3883	−1.3760
q_3	2.9800	4.2133	5.1561	4.6139

We now proceed to describe the s-wave Faddeev equations related to the Schrödinger operator (8). The general form of the equations for arbitrary total angular momentum is derived in Ref. [10].

The asymptotic dynamics of a three-body Coulomb system involves two different types of asymptotic channels according to formation of bound states in different pairs (such as $d+t\mu$ and $t+d\mu$). Each channel is most conveniently described through its own set of Jacobi coordinates $\{x_\alpha, y_\alpha, \theta_\alpha\}$, where α is the index of the bound pair. The total wave function includes all open channels. This rather complicates setting up the asymptotic conditions for scattering states, for one has to use different local maps in different regions of configuration space in order to properly deal with a variety of open channels. The basic idea of the Faddeev approach is to eliminate this problem by separating the asymptotic channels from each other. To this end, the wave function is divided into a sum of the Faddeev components. Thereby each component involves asymptotic channels due to bound states of only one pair and therefore can be completely described by one set of Jacobi coordinates.

A rigorous way to implement this idea when the long-range Coulomb interaction is involved was invented in Ref. [9]. It consists of decomposing the Coulomb potentials (9) into the two parts $V_\alpha = V_\alpha^{(s)} + V_\alpha^{(l)}$ by making use of cutoff functions ζ_α

$$V_\alpha^{(s)}(x_\alpha, y_\alpha) = V_\alpha(x_\alpha)\zeta_\alpha(x_\alpha, y_\alpha), \tag{11a}$$

$$V_\alpha^{(l)}(x_\alpha, y_\alpha) = V_\alpha(x_\alpha)[1-\zeta_\alpha(x_\alpha, y_\alpha)]. \tag{11b}$$

The cutoff functions are such that $V_\alpha^{(s)}$ coincides with the Coulomb potential V_α in the asymptotic region Ω_α corresponding to the formation of a bound state in the pair α,

$$\Omega_\alpha = \{\mathbf{x}_\alpha, \mathbf{y}_\alpha : x_\alpha/a_\alpha < (y_\alpha/b_\alpha)^{1/\nu_\alpha}, \nu_\alpha > 2\}, \tag{12}$$

when particles of the pair α are close and the spectator is far away. The constants a_α, b_α characterize the effective size of such a configuration with respect to the corresponding coordinate. In the complement of Ω_α, where there are asymptotic channels due to bound states of other pairs, the potential $V_\alpha^{(s)}$ should vanish sufficiently fast. Such behavior can be achieved, for instance, by making use of the following functional form of the cutoff proposed in Ref. [15] and used in Ref. [11]:

$$\zeta_\alpha(x_\alpha, y_\alpha) = 2\left\{1+\exp\left[\frac{(x_\alpha/a_\alpha)^{\nu_\alpha}}{(y_\alpha/b_\alpha)+1}\right]\right\}^{-1}, \tag{13}$$

where the parameters a_α, b_α are the same as in (12). Next one defines the asymptotic Hamiltonian

$$H_{\mathrm{as}} = H_0 + \sum_\alpha V_\alpha^{(l)}. \tag{14}$$

The Faddeev equations are now derived by following a general procedure [9,10] treating the potentials $V_\alpha^{(s)}$ as perturbations of the operator H_{as}. This leads to the modified Faddeev equations

$$(H_{\mathrm{as}} + V_\alpha^{(s)} - E)\psi_\alpha = -V_\alpha^{(s)} \sum_{\beta\neq\alpha} \psi_\beta, \alpha, \beta = 1,2,3 \tag{15}$$

for the Faddeev components ψ_α. It is easily seen that the sum of all three Faddeev equations yields the Schrödinger equation for the total wave function

$$\Psi = \sum_{\alpha=1}^{3} \psi_\alpha. \tag{16}$$

For the muonic-atomic systems (1) and (2) only two pairs of the particles (with $\alpha = 1,2$) have bound states. Thus the repulsive Coulomb potential V_3 can be completely included in the operator H_{as} (this corresponds to choosing $\zeta_3 \equiv 0, \psi_3 \equiv 0$). This reduces Eqs. (15) to a set of two coupled equations for the two Faddeev components $\psi_{1,2}$:

$$[H_0 + V_\alpha(x_\alpha) + V_3(x_{3\alpha}) + V_\beta^{(l)}(x_{\beta\alpha}, y_{\beta\alpha}) - E]\psi_\alpha(x_\alpha, y_\alpha, \theta_\alpha) = -V_\alpha^{(s)}(x_\alpha, y_\alpha)\psi_\beta(x_{\beta\alpha}, y_{\beta\alpha}, \theta_{\beta\alpha}), \tag{17}$$

where $\alpha, \beta = 1,2$ and $\alpha \neq \beta$. Each component depends on its own set of the Jacobi coordinates; $x_{\beta\alpha}, y_{\beta\alpha}, \theta_{\beta\alpha}$ stand for the coordinates $x_\beta, y_\beta, \theta_\beta$ expressed through $x_\alpha, y_\alpha, \theta_\alpha$ according to the transformation (5):

$$x_{\beta\alpha} = [c_{\beta\alpha}^2 x_\alpha^2 + s_{\beta\alpha}^2 y_\alpha^2 + 2c_{\beta\alpha}s_{\beta\alpha}x_\alpha y_\alpha \cos\theta_\alpha]^{1/2}, \tag{18a}$$

$$y_{\beta\alpha} = [s_{\beta\alpha}^2 x_\alpha^2 + c_{\beta\alpha}^2 y_\alpha^2 - 2c_{\beta\alpha}s_{\beta\alpha}x_\alpha y_\alpha \cos\theta_\alpha]^{1/2}, \tag{18b}$$

$$x_{\beta\alpha} y_{\beta\alpha} \cos\theta_{\beta\alpha} = (c_{\beta\alpha}^2 - s_{\beta\alpha}^2)x_\alpha y_\alpha \cos\theta_\alpha - c_{\beta\alpha}s_{\beta\alpha}(x_\alpha^2 - y_\alpha^2). \tag{18c}$$

Again, the sum of the two Faddeev equations (17) yields the Schrödinger equation with the Hamiltonian (8) for the wave function $\Psi = \psi_1 + \psi_2$. Vanishing of the coupling potential $V_\alpha^{(s)}$ away from the region Ω_α provides asymptotic decoupling of the Faddeev components.

When two particles of a system are identical, the Faddeev equations (17) can be further simplified. For the symmetric muonic atomic systems (1), particles 1 and 2 (nuclei) are identical and there are two possible parity states $\wp = \pm 1$ with respect to interchange of the nuclei $P_{21}\Psi = \wp\Psi$; depending on the spin state of the pair (1,2), $\wp = (-1)^{s_{12}}$. For a fixed parity state, the Faddeev components of Eqs. (17) are related by $P_{21}\psi_1 = \wp\psi_2$ (thereby the cutoff functions must be the same). Then Eqs. (18) imply a functional relation between the components

$$\psi_1(x, y, \theta) = \wp\psi_2(x, y, \pi - \theta), \tag{19}$$

which reduces Eqs. (17) to one equation for the component ψ_1:

$$[H_0 + V_1(x_1) + V_3(x_{31}) + V_2^{(l)}(x_{21}, y_{21}) - E]\psi_1(x_1, y_1, \theta_1) = -\wp V_1^{(s)}(x_1, y_1)\psi_1(x_{21}, y_{21}, \pi - \theta_{21}). \tag{20}$$

The component ψ_1 does not have any symmetry with respect to the interchange of the nuclei. Proper symmetry of the wave function ($P_{12}\Psi = \wp\Psi$) is enforced automatically since $\Psi = \psi_1 + \psi_2 = (1 + \wp P_{12})\psi_1$.

III. ASYMPTOTIC BOUNDARY CONDITIONS

For scattering problems the Faddeev equations are associated with appropriate asymptotic conditions. In the case of scattering in the symmetric systems $a+a\mu$ below the first excitation threshold of the muonic atom, there is only one open channel in each pair $\alpha=1,2$. The corresponding asymptotic conditions for Eq. (20) are

$$\psi_1^{(\wp)}(x_1,y_1\to\infty,\theta_1)\sim\frac{1}{p_1y_1}\varphi_1(x_1)[\sin(p_1y_1)+\tan\delta_\wp\cos(p_1y_1)], \tag{21a}$$

$$\psi_1(x_1\to\infty,y_1,\theta_1)\sim 0, \tag{21b}$$

where φ_1 is the muonic-atom ground-state wave function, $\delta_\wp$ is the phase shift, and p_1 is the momentum conjugate to the coordinate y_1. These asymptotic conditions apply to both parity states $\wp=\pm1$ (with different values of the phase shift).

The s-wave scattering cross sections for parity states $\wp=\pm1$ are given by

$$\sigma_\pm=\frac{4\pi a_\mu^2}{k_1^2}\sin^2\delta_\pm, \tag{22}$$

where

$$k_1=\mu_1p_1=\sqrt{2m_{1,23}(E-\epsilon_0)}, \tag{23}$$

$\delta_\pm$ are the corresponding phase shifts, and k_1 is the momentum in the incoming channel; $m_{1,23}=\mu_1^2/2$ is the reduced mass of the nucleus and the muonic atom and ϵ_0 is the atomic ground-state energy. The total cross section is given by the weighted average

$$\sigma_{\rm tot}=\begin{cases}\frac{1}{4}\sigma_+ + \frac{3}{4}\sigma_- & \text{for } p+p\mu,\ t+t\mu\\ \frac{2}{3}\sigma_+ + \frac{1}{3}\sigma_- & \text{for } d+d\mu.\end{cases} \tag{24}$$

Cross sections (22) correspond to fixed spin $\mathbf{s}_{12}=\mathbf{s}_1+\mathbf{s}_2$ of the two nuclei in a $a+a\mu$ system $\wp=(-1)^{s_{12}}$. The transitions between different spin states of the muonic atom $a\mu$ are also of interest. In the standard notations [5–8], the corresponding spin channels are

$$1\equiv a+a\mu(\uparrow\downarrow)\text{with } s_{23}=\begin{cases}0 & \text{for } a=p\text{or }t\\ \frac{1}{2} & \text{for } a=d,\end{cases} \tag{25a}$$

$$2\equiv a+a\mu(\uparrow\uparrow)\text{with } s_{23}=\begin{cases}1 & \text{for } a=p\text{or }t\\ \frac{3}{2} & \text{for } a=d,\end{cases} \tag{25b}$$

where $\mathbf{s}_{23}=\mathbf{s}_2+\mathbf{s}_3$ is the spin of the muonic atom $a\mu$. The cross section for a transition $i\to j$ between these channels at fixed total spin $\mathbf{S}=\mathbf{s}_1+\mathbf{s}_2+\mathbf{s}_3$ is designated $\sigma_{ij}^{(S)}$. The spin-weighted effective cross sections are given by

$$\sigma_{ij}=\sum_S\frac{2S+1}{(2s_{23}+1)(2s_1+1)}\sigma_{ij}^{(S)}. \tag{26}$$

All such cross sections can be evaluated in terms of the fixed-parity phase shifts $\delta_\pm$ of the asymptotic conditions (21). Corresponding formulas are given in the Appendix. The resulting expressions for the cross sections (26) are

$$\sigma_{21}=\frac{\pi a_\mu^2}{k_1^2}\sin^2(\delta_+-\delta_-)\times\begin{cases}\frac{1}{4} & \text{for } p+p\mu,\ t+t\mu\\ \frac{1}{12} & \text{for } d+d\mu,\end{cases} \tag{27a}$$

$$\sigma_{12}/\sigma_{21}=\begin{cases}3 & \text{for } p+p\mu,\ t+t\mu\\ 2 & \text{for } d+d\mu,\end{cases} \tag{27b}$$

$$\sigma_{11}=\sigma_{\rm tot}-\sigma_{12}, \tag{27c}$$

$$\sigma_{22}=\sigma_{\rm tot}-\sigma_{21}, \tag{27d}$$

where $\sigma_{\rm tot}$ is the total cross section given by (24).

For scattering in the asymmetric system $d+t\mu$ at energies between the $d\mu(n=1)$ and $t\mu(n=2)$ thresholds, four asymptotic channels are open: the elastic channels $d+t\mu(n=1)\to d+t\mu(n=1)$ and $t+d\mu(n=1)\to t+d\mu(n=1)$ as well as the inelastic channels $t+d\mu(n=1)\leftrightarrow d+t\mu(n=1)$. In this case, it is convenient to make use of the reactance matrix formalism. One finds two different solutions to Eqs. (17) $(\psi_1^{(\gamma)},\psi_2^{(\gamma)})$, which are labeled by the index γ $(=1,2)$ of the bound pair in the initial state,

$$\psi_\alpha^{(\gamma)}(x_\alpha,y_\alpha\to\infty,\theta_1)\sim\frac{1}{y_\alpha}\varphi_\alpha(x_\alpha)[\delta_{\gamma\alpha}\sin(p_\alpha y_\alpha)+\sqrt{p_\gamma/p_\alpha}K_{\alpha\gamma}\cos(p_\alpha y_\alpha)], \tag{28}$$

where φ_α is the muonic atomic wave function of the pair α. Thereby all the components vanish as $x_\alpha\to\infty$. The coefficients $K_{\alpha\gamma}$ are the reactance matrix elements.

As can be seen from Eq. (28), different reaction channels correspond to different Faddeev components and are asymptotically decoupled. This is a crucial point for computational efficiency of the Faddeev approach.

Note that the muonic atomic wave functions in Eqs. (21) and (28) are normalized by

$$\int_0^\infty[\varphi_\alpha(x_\alpha)]^2x_\alpha^2dx_\alpha=1. \tag{29}$$

This differs from standard normalization since the Jacobi coordinates involve the mass-dependent factors τ_α of Eq. (3a). This fact is taken into account in the asymptotic conditions (21) or (28) where the momenta p_α are related to the momenta k_α of the spectator with respect to the bound pair, according to Eq. (3b), by

$$k_\alpha=\mu_\alpha p_\alpha. \tag{30a}$$

The total three-body energy is

$$E=-\frac{q_\alpha^2}{4}+p_\alpha^2, \tag{30b}$$

where the q_α are the mass-scaled charges (9b).

The cross sections for the transitions $\gamma\rightarrow\alpha$ between the channels are given in terms of the K matrix by

$$\sigma_{\gamma\alpha}=\frac{4\pi a_\mu^2}{k_\gamma^2}\left|\left(\frac{\mathbf{K}}{1-i\mathbf{K}}\right)_{\gamma\alpha}\right|^2, \tag{31}$$

where a_μ is the muonic Bohr radius. Subscripts γ,α designate the initial and final states, respectively: 1 for $d+t\mu(n=1)$ and 2 for $t+d\mu(n=1)$.

IV. NUMERICAL PROCEDURE

Our method of solving the Faddeev equations, originally developed in Ref. [11], involves the following major steps. First, we separate off the incoming waves by representing the Faddeev components as

$$\psi_\alpha(x_\alpha,y_\alpha,\theta_\alpha)=f_\alpha(x_\alpha,y_\alpha)+\frac{1}{x_\alpha y_\alpha}\Phi_\alpha(x_\alpha,y_\alpha,\theta_\alpha), \tag{32}$$

where f_α are the incident waves $\sim\sin(p_\alpha y_\alpha)$ for the corresponding asymptotic conditions (21) and (28). Then Eqs. (17) and (20) go over into inhomogeneous equations for the functions Φ_α, which now contain only outgoing waves $\sim\cos(p_\alpha y_\alpha)$.

Then we make use of nonlinear mappings of the coordinates $\{x_\alpha,y_\alpha\}$ into new variables $\{t_\alpha,r_\alpha\}\in[0,1]\times[0,1]$,

$$x_\alpha=-\frac{1}{\lambda_\alpha}\ln(1-t_\alpha), \tag{33a}$$

$$y_\alpha=h_\alpha\left[\left(1+\frac{y_\alpha^{(m)}}{h_\alpha}\right)^{r_\alpha}-1\right]. \tag{33b}$$

Uniform grids in t_α and r_α generate nonuniform grids in x_α and y_α with point densities governed by the parameters of the mappings (33). The parameter $y_\alpha^{(m)}$ determines the maximum value of y_α, where the corresponding asymptotic condition is imposed $y_\alpha^{(m)}=y_\alpha(r_\alpha=1)$. The logarithmic mapping $t_\alpha\rightarrow x_\alpha$ is suitable to describe the bound states of muonic atoms, whereas the exponential mapping $r_\alpha\rightarrow y_\alpha$ is a reasonable choice to treat scattering dynamics along y_α.

Next the Faddeev equations (17) or (20) for the components Φ_α from (32) are written in terms of the variables $\{t_\alpha,r_\alpha,\theta_\alpha\}$. At the boundaries $t_\alpha=0,1$ $(x_\alpha=0,\infty)$, $r_\alpha=0$ $(y_\alpha=0)$, and $\theta_\alpha=0,\pi$, vanishing boundary conditions are imposed [11],

$$\Phi_\alpha|_{t_\alpha=0}=\Phi_\alpha|_{r_\alpha=0}=\partial_{t_\alpha}^n\Phi_\alpha|_{t_\alpha=1}=0 \quad \text{for } n\leqslant 1, \tag{34a}$$

$$\partial_{\theta_\alpha}\Phi_\alpha|_{\theta_\alpha=0,\pi}=0. \tag{34b}$$

At the asymptotic boundaries $r_\alpha=1$ $(y_\alpha=y_\alpha^{(m)})$ we impose the asymptotic conditions (21) and (28). Accordingly, the functions Φ_α are proportional to $\cos(p_\alpha y_\alpha)$. Thus

$$\partial_{y_\alpha}\Phi_\alpha|_{y_\alpha\rightarrow\infty}\sim-p_\alpha\tan(p_\alpha y_\alpha)\Phi_\alpha, \tag{35a}$$

$$\partial_{y_\alpha}^2\Phi_\alpha|_{y_\alpha\rightarrow\infty}\sim-p_\alpha^2\Phi_\alpha. \tag{35b}$$

Upon evaluating these relations in terms of the variable r_α, one gets boundary conditions to be imposed at $r_\alpha=1$ $(y_\alpha=y_\alpha^{(m)})$.

To reduce the resulting inhomogeneous equations to an algebraic problem, we make use of spline expansions in all variables

$$\Phi_\alpha(t_\alpha,r_\alpha,\theta_\alpha)=\sum_{l=1}^{N_x^{(\alpha)}}\sum_{m=1}^{N_y^{(\alpha)}}\sum_{n=1}^{N_\theta^{(\alpha)}}f_{lmn}^{(\alpha)}s_l(t_\alpha)s_m(r_\alpha)s_n(\theta_\alpha), \tag{36}$$

where s_i are the quintic Hermite polynomial splines defined as follows. Let an interval of a variable x be divided into K subintervals defined by the natural knots $x_0,x_1,\ldots,x_K$. The total cardinal basis of the quintic splines consists of $3K+3$ piecewise polynomials of fifth degree $\varphi_{i\sigma}$ $(i=0,1,\ldots,K;\sigma=0,1,2)$, which are nonzero on two adjacent subintervals $[x_{i-1},x_i]\cup[x_i,x_{i+1}]$. This set of functions is fixed by the continuity condition on their first and second derivatives and by the normalization at the natural knots,

$$\partial_x^\sigma\varphi_{i\sigma'}=\delta_{\sigma\sigma'} \quad \text{for } \sigma,\sigma'=0,1,2. \tag{37}$$

The explicit formulas for the spline functions are

$$\varphi_{n\sigma}(x)=(1-t)^3(x-x_n)^\sigma\times\begin{cases}6t^2+3t+1 & \text{for } \sigma=0\\ 3t+1 & \text{for } \sigma=1\\ 1/2 & \text{for } \sigma=2,\end{cases} \tag{38}$$

where $x\in[x_{n-1},x_{n+1}]$ and

$$t=(x-x_n)\times\begin{cases}(x_{n-1}-x_n)^{-1} & \text{for } x_{n-1}\leqslant x\leqslant x_n\\ (x_{n+1}-x_n)^{-1} & \text{for } x_n\leqslant x\leqslant x_{n+1}.\end{cases} \tag{39}$$

Upon substituting the spline expansion (36) into the Faddeev equations we make use of a collocation procedure with three Gaussian quadrature points per subinterval of each variable t_α, r_α, and θ_α. If there are K subintervals of a variable, the basis of quintic splines consists of $3K+3$ functions, but the collocation procedure yields only $3K$ equations. The three extra splines on the first and last subintervals are excluded by the boundary conditions (34) and (35). The resulting algebraic equation for the coefficients $f_{lmn}^{(\alpha)}$ is solved by direct matrix inversion.

V. RESULTS AND DISCUSSION

Our calculations were performed on grids of typical dimensions $N_x^{(\alpha)}\times N_y^{(\alpha)}\times N_\theta^{(\alpha)}=(12-18)\times(39-60)\times(12-18)$. The corresponding accuracy is estimated to be of order 1%. The values of the particle masses we used are $m_p=1836.1515m_e$, $m_d=3670.481m_e$, $m_t=5496.918m_e$, and $m_\mu=206.769m_e$.

A. Cross sections

Tables II–IV give our results for scattering in the symmetric systems below the $n=2$ threshold of the corresponding muonic atom. In terms of the momentum k_1 of the incident nucleus with respect to the target [see Eq. (30)], the

TABLE II. Phase shifts (in radians) and cross sections (in units of $\pi a_\mu^2 = 0.206 \times 10^{-20}$ cm^2) for $p+p\mu$ scattering as functions of the momentum k_1 (in units of a_μ^{-1}). E_1 (eV) $= 601.538 k_1^2$.

k_1	δ_+	δ_-	σ_+	σ_-	$\sigma_{\rm tot}$	σ_{21}	σ_{11}	σ_{22}
0.01	3.4287	3.1018	3207.6	63.31	849.4	257.8	76.05	591.6
0.03	3.7642	3.0150	1511.4	70.85	431.0	128.8	44.46	302.2
0.05	3.8638	2.9233	699.2	75.04	231.1	65.26	35.28	165.8
0.10	3.7891	2.6766	145.5	80.43	96.71	20.11	36.39	76.60
0.20	3.3838	2.1708	5.753	68.12	52.53	5.484	36.08	47.04
0.30	2.9540	1.7076	1.546	43.62	33.10	2.496	25.61	30.60
0.40	2.5598	1.2974	7.549	23.18	19.27	1.419	15.02	17.85
0.50	2.2109	0.9380	10.29	10.40	10.38	0.914	7.634	9.462
0.60	1.9051	0.6165	9.915	3.714	5.265	0.641	3.343	4.624
0.65	1.7807	0.4653	9.056	1.906	3.694	0.554	2.032	3.140
0.70	1.6346	0.3390	8.130	0.903	2.710	0.473	1.292	2.237
0.80	1.4000	0.0924	6.069	0.053	1.557	0.364	0.465	1.193
0.90	1.1920	−0.1245	4.263	0.076	1.123	0.289	0.256	0.834
1.00	1.0080	−0.3172	2.861	0.389	1.007	0.235	0.302	0.772
1.10	0.8435	−0.4870	1.845	0.724	1.004	0.195	0.419	0.809
1.20	0.6940	−0.6360	1.136	0.980	1.019	0.164	0.528	0.855
1.30	0.5615	−0.7710	0.671	1.149	1.030	0.140	0.611	0.890
1.40	0.4407	−0.8900	0.371	1.232	1.017	0.120	0.656	0.897
1.60	0.2334	−1.0860	0.084	1.223	0.938	0.092	0.663	0.847

thresholds are at $k_1 = 1.776 a_\mu^{-1}$ for $p+p\mu$, $k_1 = 2.545 a_\mu^{-1}$ for $d+d\mu$, and $k_1 = 3.128 a_\mu^{-1}$ for $t+t\mu$. For momentum k_1 (in units of a_μ^{-1}) given by (30) the corresponding kinetic energy is

$$E_1 \text{ (eV)} = 2 \text{ Ry} \frac{m_\mu}{m_e} p_1^2 = 2 \text{ Ry} \frac{m_\mu}{m_e} \mu_1^{-2} k_1^2, \qquad (40)$$

where Ry $= 13.605\,698$ eV and μ_1 is the reduced mass defined in Eq. (4) (see Table I for numerical values).

In Tables II–IV we present phase shifts $\delta_\pm$ of scattering in states of fixed parity $\wp = \pm 1$ with respect to the interchange of identical nuclei; $\sigma_\pm$ are the corresponding cross sections (22) and $\sigma_{\rm tot}$ is the spin-weighted total cross section (24). The cross sections σ_{ij} are the spin-weighted effective

TABLE III. Phase shifts (in radians) and cross sections (in units of $\pi a_\mu^2 = 0.206 \times 10^{-20}$ cm^2) for $d+d\mu$ scattering as functions of the momentum k_1 (in units of a_μ^{-1}). E_1 (eV) $= 308.507 k_1^2$.

k_1	δ_+	δ_-	σ_+	σ_-	$\sigma_{\rm tot}$	σ_{21}	σ_{11}	σ_{22}
0.01	6.2284	6.2480	119.9	49.50	96.46	0.960	95.82	96.1
0.03	6.1105	6.1668	131.2	59.93	107.5	0.880	106.9	107.2
0.05	5.9793	6.0742	143.3	68.87	118.5	0.898	117.9	118.2
0.10	5.6328	5.7922	146.7	88.92	127.4	0.630	127.0	127.3
0.20	4.9747	5.2232	93.28	76.10	87.55	0.378	87.30	87.42
0.30	4.3964	4.6926	40.15	44.43	41.58	0.238	41.42	41.50
0.40	3.8954	4.2176	11.71	19.36	14.26	0.157	14.16	14.21
0.50	3.4604	3.7926	1.572	5.876	3.006	0.106	2.936	2.971
0.55	3.2632	3.5993	0.195	2.582	0.990	0.090	0.930	0.960
0.60	3.0785	3.4086	0.044	0.774	0.287	0.073	0.239	0.263
0.65	2.8979	3.2303	0.551	0.074	0.392	0.063	0.350	0.371
0.70	2.7416	3.0551	1.238	0.061	0.846	0.049	0.813	0.829
0.80	2.4297	2.7401	2.667	0.955	2.096	0.036	2.072	2.084
0.90	2.1666	2.4519	3.383	1.999	2.922	0.024	2.906	2.914
1.00	1.9026	2.1996	3.576	2.616	3.256	0.021	3.241	3.249
1.10	1.6916	1.9716	3.258	2.803	3.106	0.016	3.096	3.101
1.20	1.4784	1.7416	2.754	2.698	2.735	0.012	2.727	2.731
1.30	1.3000	1.5500	2.198	2.366	2.254	0.009	2.248	2.251
1.50	0.9350	1.1950	1.151	1.538	1.280	0.007	1.275	1.278
1.60	0.7750	1.0400	0.765	1.162	0.897	0.007	0.893	0.895
1.70	0.6700	0.9000	0.534	0.849	0.639	0.005	0.636	0.637
2.00	0.2700	0.5400	0.071	0.264	0.136	0.004	0.133	0.134

TABLE IV. Phase shifts (in radians) and cross sections (in units of $\pi a_\mu^2 = 0.206 \times 10^{-20}$ cm^2) for $t+t\mu$ scattering as functions of the momentum k_1 (in units of a_μ^{-1}). E_1 (eV) $= 207.808 k_1^2$.

k_1	δ_+	δ_-	σ_+	σ_-	$\sigma_{\rm tot}$	σ_{21}	σ_{11}	σ_{22}
0.01	6.3675	6.2518	283.7	39.39	100.5	33.32	0.511	67.15
0.03	6.4844	6.1748	177.5	52.01	83.39	25.79	6.030	57.60
0.05	6.5116	6.0692	82.04	72.15	74.62	18.33	19.64	56.30
0.10	6.3995	5.7832	5.387	91.94	70.30	8.353	45.24	61.95
0.20	5.9506	5.1702	10.66	80.47	63.01	3.094	53.73	59.92
0.30	5.4441	4.5986	24.60	43.87	39.06	1.555	34.39	37.50
0.40	4.9530	4.0806	23.58	16.28	18.11	0.917	15.36	17.19
0.50	4.4934	3.6111	15.25	3.275	6.268	0.596	4.479	5.671
0.55	4.2740	3.4066	10.84	0.907	3.391	0.481	1.948	2.910
0.60	4.0692	3.1961	7.114	0.033	1.803	0.408	0.580	1.396
0.65	3.8671	2.9943	4.168	0.204	1.195	0.347	0.153	0.848
0.70	3.6866	2.7901	2.194	0.968	1.274	0.311	0.340	0.963
0.80	3.3345	2.4376	0.230	2.619	2.021	0.239	1.306	1.783
0.90	3.0126	2.1006	0.082	3.677	2.778	0.193	2.199	2.585
1.00	2.7113	1.7921	0.696	3.807	3.030	0.158	2.555	2.871
1.10	2.4406	1.5110	1.375	3.294	2.814	0.133	2.416	2.682
1.20	2.1886	1.2500	1.846	2.502	2.338	0.113	1.999	2.225
1.30	1.9566	1.0090	2.032	1.695	1.779	0.098	1.487	1.682
1.40	1.7406	0.7855	1.983	1.021	1.261	0.085	1.006	1.176
1.50	1.5355	0.5783	1.776	0.531	0.842	0.074	0.619	0.768
1.60	1.3517	0.3850	1.489	0.220	0.538	0.066	0.339	0.471
1.70	1.1790	0.2078	1.182	0.059	0.340	0.059	0.163	0.281
1.80	1.0120	0.0419	0.888	0.002	0.224	0.053	0.066	0.171
1.90	0.8600	−0.1085	0.636	0.013	0.169	0.047	0.028	0.122

cross sections (26) of transitions $i \to j$ between different spin states (25) of the muonic atom. They are given in terms of the phase shifts by Eqs. (27). All the phase shifts are fixed in the zero-energy limit by the Levinson formula $\delta_\pm = \pi N$, where N is the number of three-body bound states of total angular momentum zero; $N=1$ for $p+p\mu$ and $N=2$ for $d+d\mu$ and $t+t\mu$.

1. $p+p\mu$

Among the three symmetric muonic systems, the $p+p\mu$ scattering possesses the most striking qualitative features. This system possesses a virtual state [16] of even parity on the negative axis of the second sheet of energy that is very close to the $k_1=0$ threshold. The virtual state causes a bumplike behavior of the even-parity phase shift δ_+ near the threshold, which is shown in Fig. 1. If it were exactly at threshold, the phase shift δ_+ would go to $3\pi/2$ in the limit $k_1 \to 0$. Accordingly, an extrapolation of $\delta_+(k_1)$ from a region of not too small momenta $k_1 > 0.1$ to $k_1 = 0$ would give a value rather close to $3\pi/2$. But at small energies the threshold behavior of the phase shift abruptly changes to the usual linear form $\delta_+ = \pi N - a_+ k_1 + \cdots$, where a_+ is the corresponding scattering length. This behavior implies that the virtual state is very close to, but not exactly at, the threshold. It manifests itself in a large derivative of the phase shift at $k_1=0$, which causes a large negative value of the even-parity $p+p\mu$ scattering length. In Ref. [11] the $p+p\mu$ scattering lengths were found to be $a_+ = -29.4 a_\mu$ and $a_- = 3.45 a_\mu$.

The $p+p\mu$ virtual state is due to the mass ratio m_μ/m_p being just above the critical value at which a second even-parity bound state would appear. A tiny decrease of m_μ/m_p would move the virtual state into the discrete spectrum.

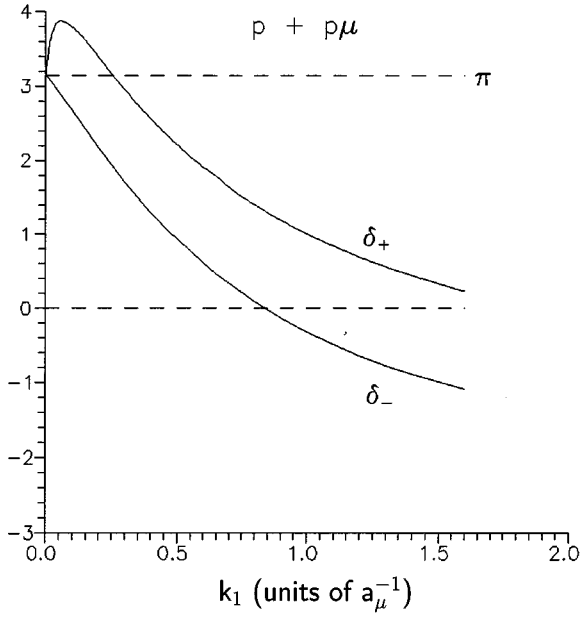

FIG. 1. Phase shifts (in radians) for $p+p\mu$ scattering in states with fixed parity $\wp = \pm 1$ with respect to the proton interchange.

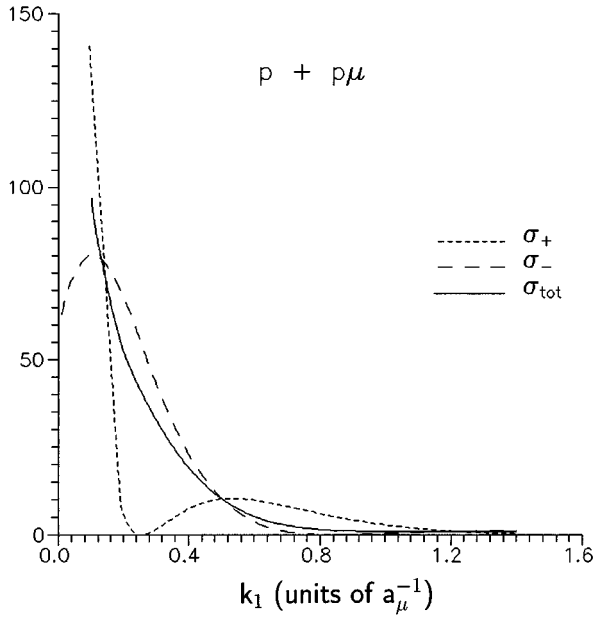

FIG. 2. Fixed-parity cross sections (22) and the spin-weighted total cross section (24) for $p+p\mu$ scattering (in units of $\pi a_\mu^2 = 0.206\times 10^{-20}$ cm^2).

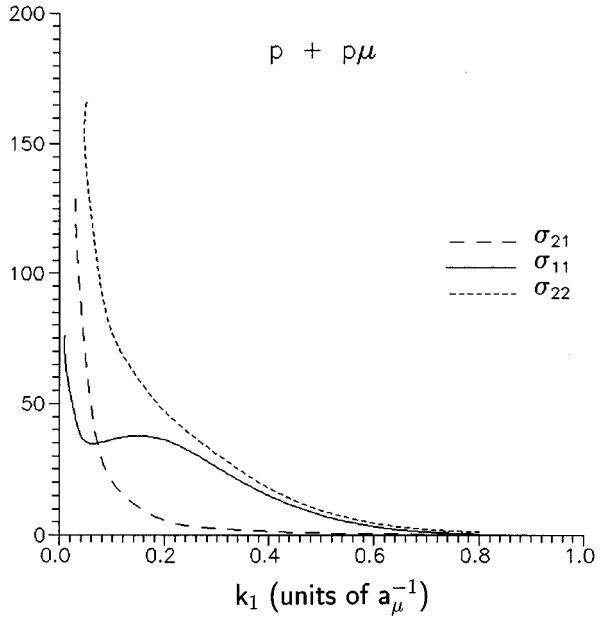

FIG. 3. Cross sections for transitions between different spin states (26) of the $p\mu$ atom in the $p+p\mu$ scattering (in units of $\pi a_\mu^2 = 0.206\times 10^{-20}$ cm^2). σ_{11} for $p+p\mu(\uparrow\downarrow)\to p+p\mu(\uparrow\downarrow)$; σ_{21} for $p+p\mu(\uparrow\uparrow)\to p+p\mu(\uparrow\downarrow)$; σ_{22} for $p+p\mu(\uparrow\uparrow)\to p+p\mu(\uparrow\uparrow)$.

Thereby the scattering length a_+ would go through $-\infty$ and then become positive, while the maximum of δ_+ in Fig. 1 would move to the origin and then disappear with further decrease of the mass ratio beyond the critical value. Such is the situation for $d+d\mu$, which has two bound states of even parity and a positive scattering length.

Another feature of interest in Fig. 1 is that in both parity states the phase shift goes through a multiple of π at nonzero energy: $\delta_+ = \pi$ at $k_1 \simeq 0.246 a_\mu^{-1}$ ($E_1 \simeq 36.4$ eV) while $\delta_- = 0$ at the rather higher energy $k_1 \simeq 0.843 a_\mu^{-1}$ ($E_1 \simeq 427$ eV). At these energies corresponding fixed-parity cross sections $\sigma_\pm$ have exact zeros.

The combination of the virtual state and the exact zeros yields an interesting structure of the fixed-parity cross sections $\sigma_\pm$ shown in Fig. 2: σ_+ has a huge maximum at the origin (due to the virtual state), rapidly decreases to zero at $k_1 \simeq 0.246 a_\mu^{-1}$, and then goes up to a second very broad maximum at $k_1 \simeq 0.56 a_\mu^{-1}$.

Upon taking the spin average, the points where the fixed-parity cross sections vanish do not show up in the total cross section $\sigma_{\rm tot}$, which has much more regular structure (Fig. 2) with a high peak at the threshold due to the virtual state with $\wp = +1$.

Cross sections for the transitions between two spin states of the $p\mu$ atom are shown in Fig. 3. All these cross sections also have profound peaks at the threshold due to the even-parity virtual state.

2. $d+d\mu$

In $d+d\mu$ scattering there is no virtual state near threshold, as can be seen from the smooth low-energy behavior of the phase shifts in Fig. 4. The zero-energy limit in the $d+d\mu$ scattering has been investigated in Ref. [11], where the following scattering lengths for this system were obtained: $a_+ = 4.81 a_\mu$, $a_- = 2.90 a_\mu$.

An interesting feature of the $d+d\mu$ system is that in a broad energy range $k_1 > 0.15 a_\mu^{-1}$ there is only a small ($\sim 10\%$) difference between the phase shifts of different parities, as seen from Fig. 4 and from the cross sections $\sigma_\pm$ in Fig. 5. Only below the first maxima of the cross sections (around $k_1 \simeq 0.12$ for both parities) is the difference apparent. Because δ_+ is close to δ_-, the cross sections for the two elastic collisions (25) σ_{11} and σ_{22}, shown in Fig. 6, are almost the same (within 1%) over the whole region be-

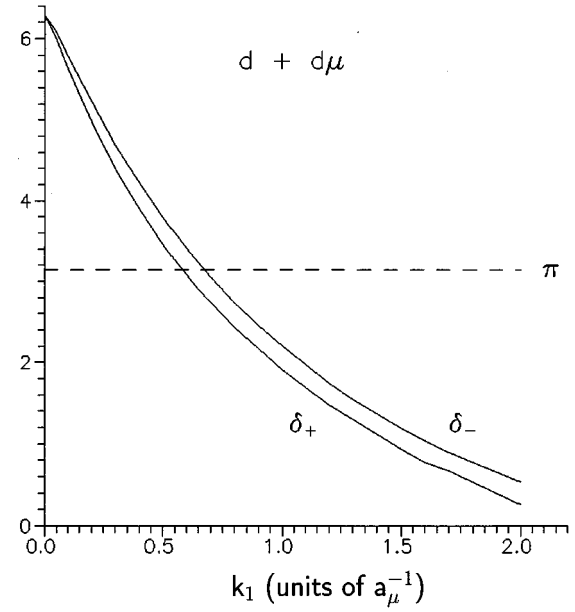

FIG. 4. Phase shifts (in radians) for $d+d\mu$ scattering in states with fixed parity $\wp = \pm 1$ with respect to the deuteron interchange.

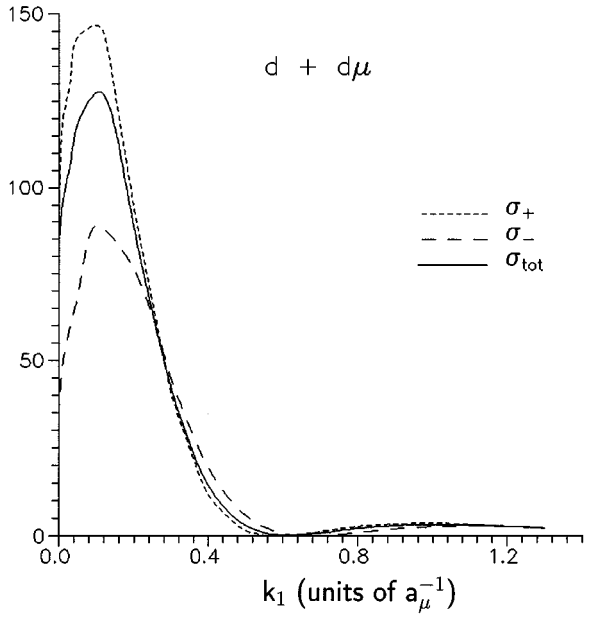

FIG. 5. Fixed-parity cross sections (22) and the spin-weighted total cross section (24) for $d+d\mu$ scattering (in units of $\pi a_\mu^2 = 0.206\times 10^{-20}$ cm^2).

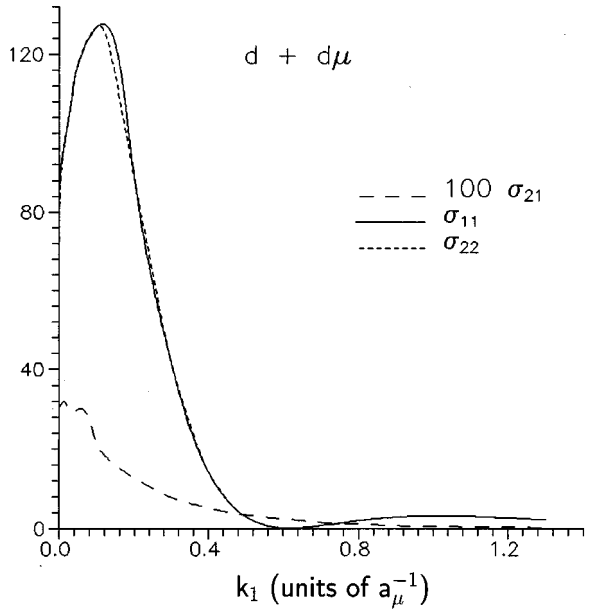

FIG. 6. Cross sections for transitions between different spin states (26) of the $d\mu$ atom in $d+d\mu$ scattering (in units of $\pi a_\mu^2 = 0.206\times 10^{-20}$ cm^2). σ_{11} for $d+d\mu(\uparrow\downarrow)\to d+d\mu(\uparrow\downarrow)$; σ_{21} for $d+d\mu(\uparrow\uparrow)\to d+d\mu(\uparrow\downarrow)$; σ_{22} for $d+d\mu(\uparrow\uparrow)\to d+d\mu(\uparrow\uparrow)$.

low the $d\mu(n=2)$ threshold, while the spin-flip cross section σ_{21} is extremely small (note the scale factor 100 for σ_{21} in Fig. 6).

As in the case of $p+p\mu$, the $d+d\mu$ phase shifts go through π in both parity states: $\delta_+ = \pi$ at $k_1 \simeq 0.583 a_\mu^{-1}$ ($E_1 \simeq 105$ eV) while $\delta_- = \pi$ at $k_1 \simeq 0.675 a_\mu^{-1}$ ($E_1 \simeq 141$ eV). At these momenta, the corresponding fixed-parity cross sections $\sigma_\pm$ have exact zeros, which result in deep and broad minima of the cross sections σ_{11} and σ_{22}, shown in Fig. 6, around $k_1 \simeq 0.6 a_\mu^{-1}$.

3. $t+t\mu$

The $t+t\mu$ system is qualitatively similar to $p+p\mu$. It also has a low-energy virtual state of even parity, as can be inferred from Fig. 7. The phase shift δ_+ has the same bumplike behavior near the threshold as the $p+p\mu$ phase shift in Fig. 1. The reason for the virtual state is also the same: the mass ratio m_μ/m_t is just above another critical value where one more (third) bound state of even parity would appear. However, compared with $p+p\mu$, the $t+t\mu$ virtual state is not as close to the threshold and the maximum in the phase shift δ_+ is broader and lower. Accordingly, the $t+t\mu$ scattering length a_+ is negative but not as large as that of $p+p\mu$. It is estimated to be about $-12a_\mu$.

Also, as in the $p+p\mu$ scattering, there are points where the $t+t\mu$ fixed-parity cross sections vanish. In Fig. 7 the phase shift δ_+ crosses 2π at $k_1 \simeq 0.126 a_m^{-1}$ ($E_1 \simeq 3.3$ eV) and π at $k_1 \simeq 0.841 a_m^{-1}$ ($E_1 \simeq 147$ eV) while δ_- goes through π at $k_1 \simeq 0.614 a_m^{-1}$ ($E_1 \simeq 78$ eV). Note that the even parity state of $t+t\mu$ has two such points, while $p+p\mu$ and $d+d\mu$ each have only one.

Interplay of the virtual state and exact zeros yields an interesting structure of the fixed-parity cross sections $\sigma_\pm$ shown in Fig. 8. It is quite similar to the behavior of the $p+p\mu$ cross sections on Fig. 2, with a profound peak of σ_+ at the threshold due to the virtual state and further oscillatory behavior with two more maxima.

Note also the unusual structure of the cross section σ_{22} in Fig. 9 between $k_1=0$ and $k_1=0.25$ and an interesting fact that at low energies $k_1 < 0.03 a_\mu^{-1}$ the total cross section $\sigma_{\rm tot}$ is about equal to the spin-flip cross section $\sigma_{12} = 3\sigma_{21}$ (see Table IV). Hence the cross section $\sigma_{11} = \sigma_{\rm tot} - \sigma_{12}$ becomes

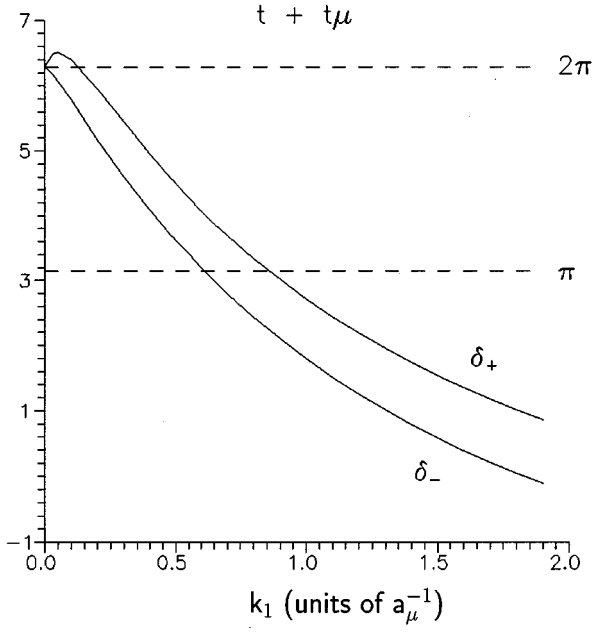

FIG. 7. Phase shifts (in radians) for $t+t\mu$ scattering in states with fixed parity $\wp = \pm 1$ with respect to the triton interchange.

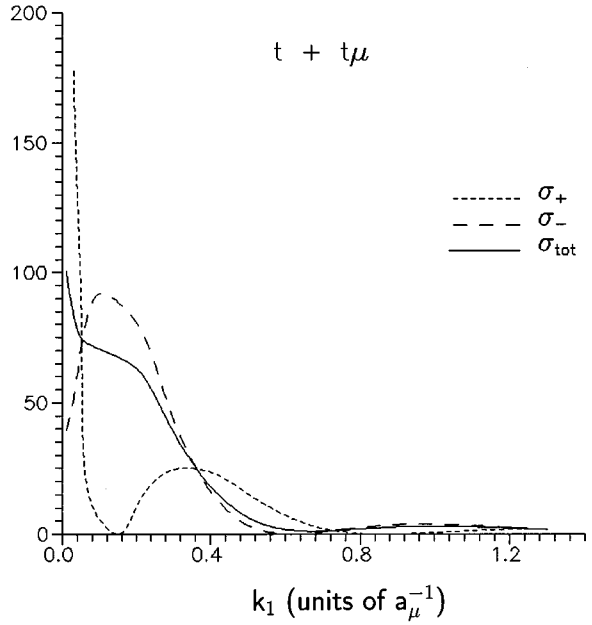

FIG. 8. Fixed-parity cross sections (22) and the spin-weighted total cross section (24) for $t+t\mu$ scattering (in units of $\pi a_\mu^2 = 0.206\times 10^{-20}$ cm^2).

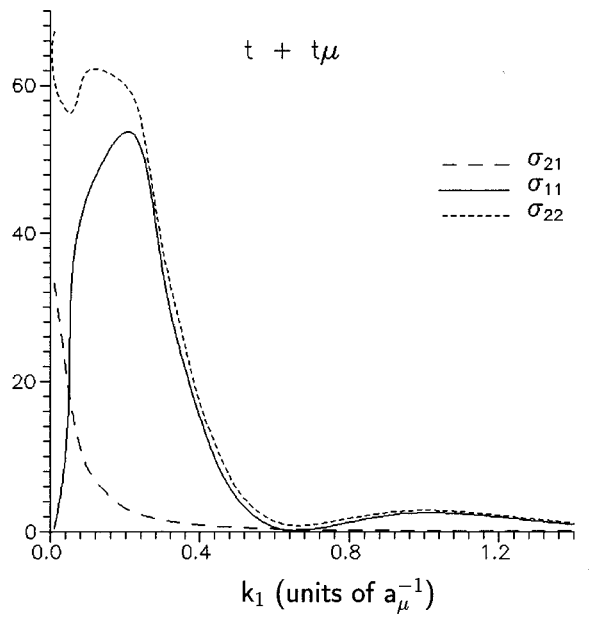

FIG. 9. Cross sections for transitions between different spin states (26) of the $t\mu$ atom in $t+t\mu$ scattering (in units of $\pi a_\mu^2 = 0.206\times 10^{-20}$ cm^2). σ_{11} for $t+t\mu(\uparrow\downarrow)\to t+t\mu(\uparrow\downarrow)$; σ_{21} for $t+t\mu(\uparrow\uparrow)\to t+t\mu(\uparrow\downarrow)$; σ_{22} for $t+t\mu(\uparrow\uparrow)\to t+t\mu(\uparrow\uparrow)$.

very small in the zero-energy limit, in sharp contrast to the low-energy behavior of σ_{22} and also to that of the $p+p\mu$ cross sections σ_{11} and σ_{12}. The reason is that the zero-energy peak of $\sigma_{\rm tot}$ is compensated by a resonancelike increase of the spin-flip cross sections σ_{12} and σ_{21} near the threshold, as seen in Fig. 9.

4. $d+t\mu$

Tables V and VI show our results for scattering in the asymmetric system $d+t\mu$ below the $t\mu(n=2)$ threshold. Reference [6] is the most extensive calculation in the adiabatic representation making use of hundreds of basis functions. Reference [7] exploits an improved version of a simple two-state adiabatic approximation. Reference [17] is a recent calculation by the coupled-rearrangement-channel method [18]. We have fair overall agreement with all these calculations.

Very close to the $d\mu(n=1)$ threshold, at $E_2<0.4$ eV, calculations become somewhat delicate, for the effective sizes of the channels $d+t\mu$ and $t+d\mu$ are very different. Kinetic energy in the $t+d\mu$ channel is very small, so that the asymptotic dynamics is governed by the long-range polarization potential between t and the $d\mu$ atom. As a result, in this channel asymptotic behavior of the wave function is achieved at very large separation ($\sim 150a_\mu - 200a_\mu$) between t and $d\mu$. But in the $d+t\mu$ channel the energy is not small and the corresponding asymptotic behavior begins at rather smaller distances ($\sim 60a_\mu$). Because in the Faddeev equations the channels are separated in different components of the wave function, we can easily deal with this situation by making use of different grids in y_1 and y_2 with different asymptotic parameters $y_\alpha^{(m)}$. This is an illustration of the computational flexibility of the Faddeev method.

The region of greatest interest is that around $E_2=28$ eV, where the K matrix has a singular behavior. As we shall show below, that is because one of the eigenphase shifts of the S matrix goes through $\pi/2(\mathrm{mod}\,\pi)$ in this region, so that its tangent is singular. This does not show up in the cross sections, but greatly affects the fusion-in-flight reaction.

B. Fusion in flight

A characteristic feature of scattering in the muonic atomic systems is the enhanced fusion-in-flight reactions

$$\left.\begin{matrix} d+t\mu \\ t+d\mu \end{matrix}\right\} \to {}^4\mathrm{He}+n+\mu^- \tag{41}$$

and

$$p+p\mu \to d+e^+ +\bar{\nu}_e+\mu^-, \tag{42a}$$

TABLE V. K-matrix and the s-wave cross sections (in units of 10^{-19} cm^2) for $d+t\mu\to d+t\mu$ scattering at kinetic energies E_1 (in eV) below the $d\mu$ threshold.

	K matrix		σ_{11}	
E_1	present	[6]	present	[6]
0.1	−0.0875	−0.08560	1.628	1.567
0.5	−0.220	−0.2206	1.975	1.999
1.0	−0.335	−0.3363	2.158	2.188
10.0	−2.153	−2.175	1.763	1.778
20.0	50.83	45.17	1.072	1.076
30.0	28.42	28.12	0.636	0.6374
40.0	1.497	1.485	0.371	0.3705

TABLE VI. K-matrix and the s-wave cross sections (in units of 10^{-20} cm^2) for $t+d\mu$ and $d+t\mu$ scattering at kinetic energies E_2 and E_1 (in eV), respectively, above the $d\mu$ threshold. The cross sections are denoted σ_{11} for $d+t\mu \to d+t\mu$, σ_{12} for $d+t\mu \to t+d\mu$, σ_{21} for $t+d\mu \to d+t\mu$, and σ_{22} for $t+d\mu \to t+d\mu$.

E_2	E_1	Reference	K_{11}	K_{21}	K_{22}	σ_{11}	σ_{12}	σ_{21}	σ_{22}
0.04	48.081	present	1.047	−0.0289	−0.0224	2.333	0.00178	2.097	2.741
		[6]	1.080	−0.02921	−0.02348	2.428	0.001775	2.092	3.036
		[17]				2.299		2.206	3.721
0.1	48.141	present	1.044	−0.0359	−0.0408	2.322	0.00274	1.296	3.611
		[6]	1.077	−0.03632	−0.04356	2.419	0.002745	1.296	4.148
		[7]	1.033	−0.0442	−0.0416	2.294	0.00419	1.983	3.805
		[17]				2.289		1.374	4.520
0.4	48.441	present	1.030	−0.0489	−0.108	2.276	0.00507	0.603	6.197
		[6]	1.064	−0.04978	−0.1145	2.374	0.005128	0.6088	7.020
		[17]				2.245		0.6428	7.016
1.0	49.041	present	1.003	−0.0592	−0.208	2.189	0.00730	0.352	8.855
		[6]	1.038	−0.0605	−0.2165	2.288	0.007420	0.3567	9.646
		[7]	0.994	−0.0732	−0.213	2.164	0.0112	0.539	9.312
		[17]				2.162		0.3754	9.569
4.0	52.041	present	0.893	−0.0833	−0.562	1.826	0.0120	0.153	12.70
		[6]	0.9202	−0.08341	−0.5765	1.907	0.01168	0.1491	13.31
		[17]				1.794		0.1591	13.33
6.0	54.041	present	0.828	−0.0957	−0.772	1.615	0.0134	0.118	13.13
		[6]	0.8515	−0.09563	−0.7984	1.686	0.01295	0.1145	13.64
		[17]				1.580		0.1226	13.67
10.0	58.041	present	0.707	−0.122	−1.238	1.240	0.0143	0.0814	12.72
		[6]	0.7314	−0.1244	−1.261	1.309	0.01432	0.08155	13.02
		[7]	0.692	−0.152	−1.263	1.208	0.0217	0.124	12.87
		[17]				1.216		0.08827	13.05
20.0	68.041	present	0.458	−0.320	−3.927	0.590	0.0158	0.0528	9.812
		[6]	0.4879	−0.3108	−3.835	0.6537	0.01536	0.05135	9.878
		[7]	0.443	−0.390	−3.925	0.580	0.0234	0.0782	9.756
		[17]				0.5896		0.05601	9.837
22.0	70.041	present	0.417	−0.405	−5.191	0.506	0.0148	0.0464	9.158
		[17]				0.5017		0.05252	9.196
24.0	72.041	present	0.369	−0.608	−7.863	0.434	0.0148	0.0436	8.563
		[17]				0.4239		0.04955	8.579
26.0	74.041	present	0.296	−1.133	−14.89	0.365	0.0144	0.0404	7.993
		[17]				0.3552		0.04699	7.990
27.0	75.041	present	0.214	−2.020	−26.58	0.337	0.0144	0.0393	7.720
		[6]	0.2035	−2.325	−29.51	0.3709	0.01539	0.04205	7.789
28.0	76.041	present	−0.383	−9.791	−128.3	0.327	0.0144	0.0383	7.452
		[6]	−0.8140	−15.03	−190.7	0.3397	0.01538	0.04106	7.517
		[17]				0.2948		0.04476	7.430

TABLE VI. (*Continued*).

E_2	E_1	Reference	K_{11}	K_{21}	K_{22}	σ_{11}	σ_{12}	σ_{21}	σ_{22}
30.0	78.041	present	0.435	1.620	21.26	0.241	0.0144	0.0367	6.937
		[6]	0.4643	1.581	19.99	0.2835	0.01535	0.03925	6.995
		[17]				0.2420		0.04277	6.899
32.0	80.041	present	0.343	0.761	9.818	0.199	0.0146	0.0358	6.447
		[17]				0.1960		0.04097	6.399
35.0	83.041	present	0.277	0.437	5.558	0.143	0.0145	0.0337	5.766
		[6]	0.3012	0.4462	5.526	0.1706	0.01517	0.03540	5.815
40.0	88.041	present	0.195	0.265	3.142	0.0714	0.0151	0.0326	4.723
		[6]	0.2186	0.2736	3.272	0.09137	0.01493	0.03233	4.802
		[17]				0.06963		0.03527	4.683
50.0	98.041	present	0.0643	0.170	1.757	0.00590	0.0152	0.0293	3.139
		[6]	0.08720	0.1692	1.810	0.01230	0.01448	0.02795	3.216
		[7]	0.0605	0.201	1.750	0.00419	0.0213	0.0410	3.111
		[17]				0.005685		0.03039	3.092
60.0	108.041	present	−0.0489	0.129	1.212	0.00645	0.0132	0.0233	2.064
		[17]				0.007099		0.02683	1.979
80.0	128.041	present	−0.255	0.106	0.643	0.105	0.0123	0.0193	0.764
		[17]				0.1078		0.02210	0.7054
100.0	148.041	present	−0.452	0.105	0.325	0.245	0.0118	0.0171	0.203
		[7]	−0.473	0.127	0.310	0.263	0.0169	0.0246	0.187
		[17]				0.2498		0.01907	0.1744

$$d+d\mu\rightarrow\begin{cases}t+p+\mu^-\\ {}^3\mathrm{He}+n+\mu^-,\end{cases} \tag{42b}$$

$$t+t\mu\rightarrow{}^4\mathrm{He}+2n+\mu^-. \tag{42c}$$

To a good approximation (for comparison, a multichannel resonating-group treatment of the nuclear degrees of freedom in the $dt\mu$ system was made in Ref. [19]), the normalized rate of the fusion in flight is just

$$\lambda_f=N_0A\rho_f, \tag{43}$$

where $N_0=4.25\times10^{22}$ atoms/cm^3 is the density of liquid hydrogen, A is the nuclear constant given in Table VII, and ρ_f is the probability for the nuclei to coincide. The three-body complication resides in the last factor, which is given by

$$\rho_f=\int|\Psi(\mathbf{r}_1,\mathbf{r}_2,\mathbf{r}_3)|^2\delta(\mathbf{r}_1-\mathbf{r}_2)d\mathbf{r}_3, \tag{44}$$

where Ψ is the wave function of the corresponding scattering process and the $\mathbf{r}_i$ are the position vectors of the particles indexed as in Eqs. (3) with $\alpha=3$ being the index of the muon. The wave function is normalized to unit incoming wave in the corresponding channel, e.g.,

$$\Psi\sim\varphi_1(\mathbf{r}_3-\mathbf{r}_2)\frac{\sin(k_1R+\delta)}{k_1R}+\cdots, \tag{45}$$

where R is the distance from the incoming nucleus to the center-of-mass of the target muonic atom and the ellipsis stands for the contribution of other open channels. Note that the effective density (44) can be interpreted as a Jost function related to fusion-in-flight reactions [20,21].

The nuclear constants in Table VII are determined from the experimental [22,23] astrophysical S factors in the $E\rightarrow0$ limit,

TABLE VII. Nuclear constants for fusion reactions in the muonic-atomic systems. A (cm^3/s)$=1.4038\times10^{-15}S_0$ (MeV b)$/M_r$ (a.m.u.).

Nuclei	Reference	S_0 (MeV b)	M_r (a.m.u.)	A (cm^3/s)
pp	[22]	$3.36\times10^{-25}\pm10\%$	0.5037	9.36×10^{-40}
dd	[22]	$2\times5.30\times10^{-2}\pm10\%$	1.0068	1.48×10^{-16}
tt	[23]	0.210 ± 0.018	1.5078	1.96×10^{-16}
pd	[22]	$2.50\times10^{-7}\pm10\%$	0.6714	5.23×10^{-22}
pt	[22]	$2.56\times10^{-6}\pm20\%$	0.7551	4.76×10^{-21}
dt	[22]	$11.0\pm20\%$	1.2074	1.28×10^{-14}

TABLE VIII. Effective densities and rates of fusion in flight in the symmetric muonic-atomic systems as functions of the momentum k_1 (in units of a_μ^{-1}).

	$p+p\mu$		$d+d\mu$		$t+t\mu$	
k_1	ρ_f	λ_f (s^{-1})	ρ_f	λ_f (s^{-1})	ρ_f	λ_f (s^{-1})
0.01	0.379×10^{0}	0.151×10^{-16}	0.990×10^{-3}	0.623×10^{4}	0.264×10^{-3}	0.220×10^{4}
0.03	0.254×10^{0}	0.101×10^{-16}	0.962×10^{-3}	0.605×10^{4}	0.208×10^{-3}	0.173×10^{4}
0.05	0.154×10^{0}	0.613×10^{-17}	0.924×10^{-3}	0.581×10^{4}	0.156×10^{-3}	0.130×10^{4}
0.10	0.509×10^{-1}	0.202×10^{-17}	0.903×10^{-3}	0.568×10^{4}	0.831×10^{-4}	0.692×10^{3}
0.20	0.853×10^{-2}	0.339×10^{-18}	0.116×10^{-2}	0.730×10^{4}	0.187×10^{-4}	0.156×10^{3}
0.30	0.438×10^{-3}	0.174×10^{-19}	0.814×10^{-5}	0.512×10^{2}	0.370×10^{-5}	0.308×10^{2}
0.40	0.209×10^{-2}	0.831×10^{-19}	0.309×10^{-3}	0.194×10^{4}	0.117×10^{-3}	0.975×10^{3}
0.50	0.105×10^{-1}	0.418×10^{-18}	0.364×10^{-3}	0.229×10^{4}	0.447×10^{-4}	0.372×10^{3}
0.60	0.141×10^{-1}	0.561×10^{-18}	0.381×10^{-3}	0.240×10^{4}	0.240×10^{-4}	0.200×10^{3}
0.80	0.105×10^{-1}	0.418×10^{-18}	0.419×10^{-3}	0.264×10^{4}	0.106×10^{-4}	0.883×10^{2}
1.00	0.730×10^{-2}	0.290×10^{-18}	0.543×10^{-3}	0.342×10^{4}	0.180×10^{-5}	0.150×10^{2}

$$A=\frac{\hbar}{\pi e^2 M_r}S_0, \tag{46}$$

where M_r is the reduced mass of the nuclei. For the s-wave reaction (42b) the rates of the two fusion channels are very nearly equal due to the proton-neutron "mirror symmetry." This accounts for the factor 2 for the dd value of S_0 in Table VII, so that Eq. (43) gives the total fusion-in-flight rate for the two channels.

If one neglects the Coulomb interaction between the nuclei and the muon, then the energy dependence of the effective density $\rho_f(E)$ is given by the Gamov factor $C_0^2(\eta)$, where η is corresponding Coulomb parameter [22]. This approximation works well at high collision energies (in the keV range) and is sometimes used to extrapolate to the threshold limit. However, a numerical study by Melezhik [20] using a two-state adiabatic approximation revealed qualitative deviation from the Gamov formula in the low-energy domain below 100 eV. Froelich *et al.*, [24] using semiclassical, adiabatic, and nonadiabatic descriptions, have also discussed amplifications of $dt\mu$ fusion in flight.

For the symmetric systems, the scattering wave function in (44) with appropriate asymptotic conditions is built up of the wave functions $\Psi_\pm=(1\pm P_{12})\psi_1^{(\pm)}$ of fixed parity. The Faddeev component $\psi_1^{(\pm)}$ is fixed by the asymptotic conditions (21). Then the wave function in (44) is

$$\Psi=\frac{1}{2}\cos\delta(\Psi_+ +\Psi_-)\sim\varphi_1(x_1)\sin(p_1y_1+\delta) +K_{21}\cos\delta\varphi_1(x_2)\cos(p_2y_2), \tag{47}$$

where

$$\tan\delta=\frac{1}{2}(\tan\delta_+ +\tan\delta_-) \tag{48a}$$

and

$$K_{21}=\frac{1}{2}(\tan\delta_+ -\tan\delta_-). \tag{48b}$$

At $\mathbf{r}_1=\mathbf{r}_2$, Eqs. (5) imply $\mathbf{x}_3=0$, $\mathbf{x}_1=s_{13}\mathbf{y}_3$, $\mathbf{x}_2=s_{23}\mathbf{y}_3$, $\mathbf{y}_1=c_{13}\mathbf{y}_3$, and $\mathbf{y}_2=c_{23}\mathbf{y}_3$. From these relations it follows that $\Psi_-=0$ at $\mathbf{r}_1=\mathbf{r}_2$. Hence the nonzero contribution to the integral (44) comes only from the Ψ_+ component of the wave function (47). The effective density can be written in terms of the corresponding Faddeev component as

$$\rho_f=\left(\frac{\tau_1}{\mu_3}\right)^3\cos^2\delta \times\int_0^\infty[\psi_1^{(+)}(x_1=|s_{13}|y_3,y_1=|c_{13}|y_3,\theta_1=\pi)]^2y_3^2dy_3, \tag{49}$$

where δ is the phase shift (48a) and $\psi_1^{(+)}$ is the solution to the Faddeev equation (20) for the $\wp=+1$ state normalized by the asymptotic conditions (21). The mass-dependent factor in front of the integral comes from the relations (3) between the Jacobi vectors and the physical distances $y_1=\mu_1R$ and $x_1=\tau_1|\mathbf{r}_3-\mathbf{r}_2|$.

Table VIII and Fig. 10 present the effective densities and rates of the fusion-in-flight reactions (42). For $p+p\mu$ and $t+t\mu$ collisions the effective density near the threshold increases greatly (see Fig. 10), especially for $p+p\mu$ scattering. This is related to the existence of the $p+p\mu$ and $t+t\mu$ virtual states that we discussed above. The $p+p\mu$ virtual state is closer to threshold than that of $t+t\mu$; accordingly, the $p+p\mu$ effective density increases more sharply than that of $t+t\mu$. The $d+d\mu$ system does not have such a virtual state, and near-threshold enhancement of its effective density is not so dramatic.

Our results for $p+p\mu$ fusion in flight are in good agreement with those of Ref. [20], where the problem was studied via a simple two-state adiabatic approximation. In particular, in Ref. [20] the $p+p\mu$ effective density (called there the "Jost function") was found to increase rapidly near the threshold and to have a minimum around $E_1\simeq70$ eV ($k_1\simeq0.34a_\mu^{-1}$), just as in our calculations (see Fig. 10).

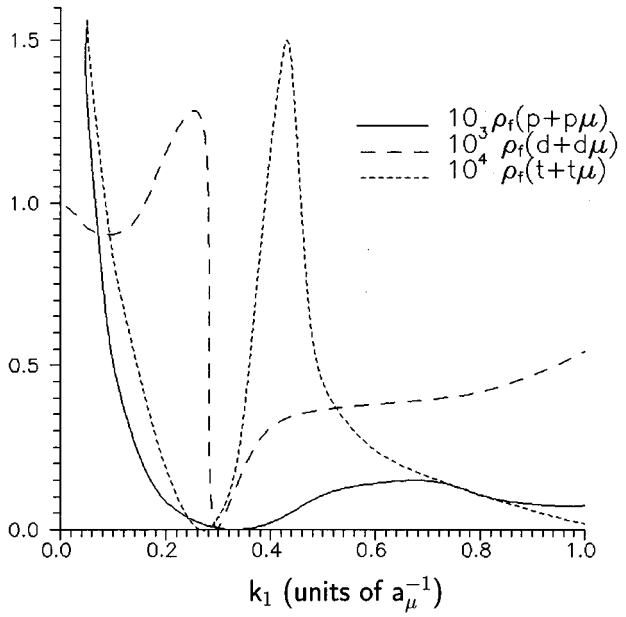

FIG. 10. Effective densities (49) of the fusion-in-flight reactions (42) in $p+p\mu$, $d+d\mu$, and $t+t\mu$ scattering.

In all three cases shown in Fig. 10 the effective densities have deep minima accompanied by nearby maxima. In fact, at the minima the effective densities are exactly zero if the g and u symmetries are assumed to be exact (i.e., if the hyperfine splitting is neglected) [25]. This behavior can be understood in terms of the phase shifts $\delta_\pm$; the positions of the zeros of the effective densities are given by the condition

$$\delta_-(k_1)=\frac{\pi}{2}(\mathrm{mod}\ \ \pi), \tag{50}$$

while the maxima correspond to

$$\delta_+(k_1)=\frac{\pi}{2}(\mathrm{mod}\ \ \pi). \tag{51}$$

Indeed, when $\cos\delta_\pm=0$ we have $\cos\delta=0$ and the asymptotic form (47) can be recast as

$$\Psi\sim\varphi_1(x_1)\cos(p_1y_1)+\epsilon\varphi_1(x_2)\cos(p_2y_2), \tag{52}$$

where

$$\epsilon=\frac{\tan\delta_+-\tan\delta_-}{\tan\delta_++\tan\delta_-}=\begin{cases}-1 & \text{for } \delta_-=\dfrac{\pi}{2}(\mathrm{mod}\ \ \pi)\\ +1 & \text{for } \delta_+=\dfrac{\pi}{2}(\mathrm{mod}\ \ \pi).\end{cases} \tag{53}$$

Thus, if $\cos\delta_-=0$ the asymptotic form (52) is antisymmetric with respect to interchange of the nuclear coordinates. This implies that Ψ is also antisymmetric, so that $\Psi=0$ at $\mathbf{r}_1=\mathbf{r}_2$ and the effective density (44) vanishes.

If $\cos\delta_+=0$, the asymptotic form (52) and therefore the wave function Ψ are symmetric with respect to the nuclear interchange and the effective density has a maximum. In general ($\cos\delta_\pm\neq0$), the wave function is a mixture of symmetric and antisymmetric components.

TABLE IX. Positions of zeros and maxima, given by Eqs. (50) and (51), of the effective densities of fusion in flight in the symmetric muonic-atomic systems.

	Positions of zeros		Positions of maxima	
System	k_1 (a_μ^{-1})	E_1 (eV)	k_1 (a_μ^{-1})	E_1 (eV)
$p+p\mu$	0.3335	66.90	0.7272	256.4
$d+d\mu$	0.2963	27.09	0.2454	18.58
	1.289	512.6	1.157	413.0
$t+t\mu$	0.2801	16.30	0.4524	42.53
	1.079	241.9	1.483	457.0

Equations (50) and (51) allow us to get accurate positions of the zeros and maxima of the effective densities by interpolating the phase shifts given in Tables II–IV; the results are presented in Table IX. Note that the first maximum gets sharper with an increase of the nuclear mass (see Fig. 10). Now we shall see that a similar effect exists in the $d+t\mu$ fusion-in-flight reaction.

For $d+t\mu$ (denoted $\gamma=1$) and $t+d\mu$ (denoted $\gamma=2$) the effective densities (44) are

$$\rho_f^{(\gamma)}=\frac{\tau_\gamma^3}{p_\gamma^2\mu_3^3(1+K_{\gamma\gamma}^2)}\times\int_0^\infty[\,\psi_1^{(\gamma)}(x_1=|s_{13}|y_3,y_1=|c_{13}|y_3,\theta_1=\pi)+\psi_2^{(\gamma)}(x_2=|s_{23}|y_3,y_2=|c_{23}|y_3,\theta_2=0)\,]^2y_3^2dy_3, \tag{54}$$

where $\psi_\alpha^{(\gamma)}$ are the Faddeev components normalized by the asymptotic conditions (28) and $K_{\gamma\gamma}$ are the diagonal elements of the reactance matrix.

Table X and Fig. 11 present our results for fusion in flight in $d+t\mu$ collisions. The effective density $\rho_f^{(2)}$ of the reaction $t+d\mu\to{}^4\mathrm{He}+n+\mu^-$ has smooth behavior while the $\rho_f^{(1)}$ of the reaction $d+t\mu\to{}^4\mathrm{He}+n+\mu^-$ has a profound peak. This is in agreement with Ref. [20], where the peak was discovered.

The origin of this peak, as for the similar maxima in the symmetric systems, can be explained approximately in terms of the eigenphase shifts $\delta_\pm$ of the S matrix. They are expressed in terms of the reactance matrix by

$$\tan\delta_\pm=\frac{1}{2}(K_{11}+K_{22})\pm\sqrt{\frac{1}{4}(K_{11}-K_{22})^2+K_{12}^2}. \tag{55}$$

Their behavior near the peak is shown in Fig. 12. The peak is due to the fact that the eigenphase shift δ_+ goes through $\pi/2$, just as in the symmetric systems. In fact, the peak for

TABLE X. Effective densities (ρ_f) and rates (λ_f) for the fusion-in-flight reactions $d+t\mu \rightarrow {}^4\mathrm{He}+n+\mu^-$ (index 1) and for $t+d\mu \rightarrow {}^4\mathrm{He}+n+\mu^-$ (index 2).

E_1 (eV)	$\rho_f^{(1)}$ (10^{-4})	$\lambda_f^{(1)}$ (s^{-1})	E_2 (eV)	$\rho_f^{(2)}$ (10^{-4})	$\lambda_f^{(2)}$ (s^{-1})
0.1	2.072	0.113×10^6			
0.5	1.927	0.105×10^6			
1.0	1.831	0.996×10^5			
10.0	1.339	0.728×10^5			
20.0	1.133	0.616×10^5			
30.0	1.023	0.557×10^5			
48.08	0.920	0.500×10^5	0.04	1.394	0.758×10^5
48.14	0.943	0.513×10^5	0.1	1.359	0.739×10^5
48.44	0.969	0.527×10^5	0.4	1.272	0.692×10^5
49.44	0.915	0.498×10^5	1.0	1.149	0.625×10^5
52.04	0.877	0.477×10^5	4.0	0.941	0.512×10^5
54.04	0.843	0.459×10^5	6.0	0.893	0.486×10^5
58.04	0.757	0.412×10^5	10.0	0.790	0.430×10^5
68.04	0.527	0.287×10^5	20.0	0.666	0.362×10^5
70.04	0.440	0.239×10^5	22.0	0.641	0.349×10^5
72.04	0.282	0.153×10^5	24.0	0.625	0.340×10^5
74.04	0.056	0.305×10^4	26.0	0.606	0.330×10^5
75.04	0.078	0.424×10^4	27.0	0.599	0.326×10^5
76.04	21.11	0.115×10^7	28.0	0.594	0.323×10^5
76.32	62.59	0.340×10^7	28.28	0.592	0.322×10^5
78.04	2.816	0.153×10^6	30.0	0.580	0.316×10^5
80.04	1.554	0.845×10^5	32.0	0.572	0.311×10^5
83.04	1.139	0.620×10^5	35.0	0.557	0.303×10^5
88.04	0.983	0.535×10^5	40.0	0.548	0.298×10^5
98.04	0.817	0.444×10^5	50.0	0.500	0.272×10^5
108.04	0.712	0.387×10^5	60.0	0.461	0.251×10^5
128.04	0.631	0.343×10^5	80.0	0.414	0.225×10^5
148.04	0.580	0.316×10^5	100.0	0.377	0.205×10^5

$d+t\mu$ is very similar to the sharp maximum of the effective density for $t+t\mu$ at $E_1=42.5$ eV. It is also accompanied by a minimum in ρ_f at slightly lower collision energy. Also, as in the $t+t\mu$ case, there is some amplification of the rate of the fusion in flight for $d+t\mu$ system towards the $t\mu$ threshold.

Interpolating the eigenphase shift δ_+ for $d+t\mu$ enables us to estimate accurately the position of the peak to be $E_1=76.32$ eV. The peak rate 3.40×10^6 s^{-1} for fusion in flight is about 7.5 times faster than the rate of muon decay $0.455\times10^6 s^{-1}$, though still much slower than the slowing-down rate ($\sim5\times10^{10}$ s^{-1} [26]) for the $t\mu$ atom in a normal *d-t* mixture. This fusion rate is twice that given by the calculation of Ref. [20] ($\sim1.7\times10^5$ s^{-1} before rounding). Our value for $d+t\mu$ fusion in flight in the $E_1\rightarrow0$ limit, 1.14×10^5 s^{-1}, is also about twice as large as that in Ref. [20] (0.5×10^5 s^{-1}) and may also be compared with the values reported in other calculations, 1.2×10^5 s^{-1} [21] and 2.1×10^5 s^{-1} [27].

We would like to emphasize that the structure in the fusion-in-flight rates is not due to asymptotic resonant scattering states at these energies but is rather a symmetry effect, as is clear from the above analysis. The periodic oscillations predicted in Ref. [20] are not seen, but their possibility is not ruled out since they might have recurrence periods exceeding the maximum collision energy treated in the present calculations.

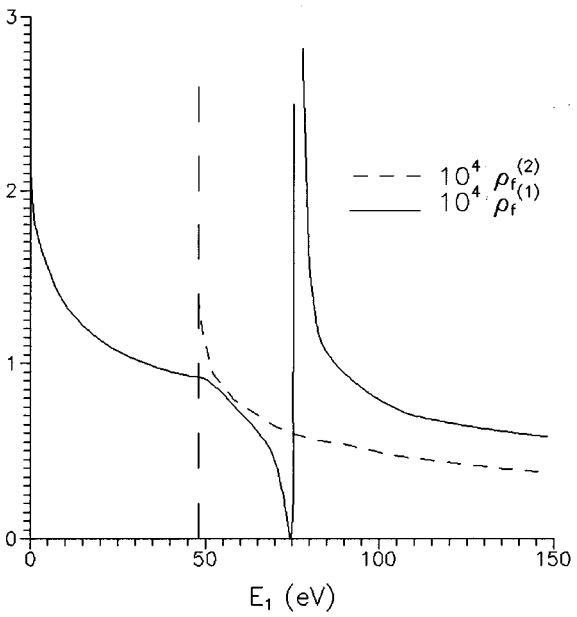

FIG. 11. Effective densities (54) of the fusion-in-flight reactions $d+t\mu \rightarrow {}^4\mathrm{He}+n+\mu^-(\rho_f^{(1)})$ and $t+d\mu \rightarrow {}^4\mathrm{He}+n+\mu^-(\rho_f^{(2)})$. The energy E_1 is measured with respect to the $t\mu(n=1)$ threshold. Vertical line at $E_1=48.042$ eV shows the $d\mu(n=1)$ threshold.

ACKNOWLEDGMENTS

We are grateful to V. S. Melezhik and V. V. Korobov for several helpful discussions. This work was made possible by

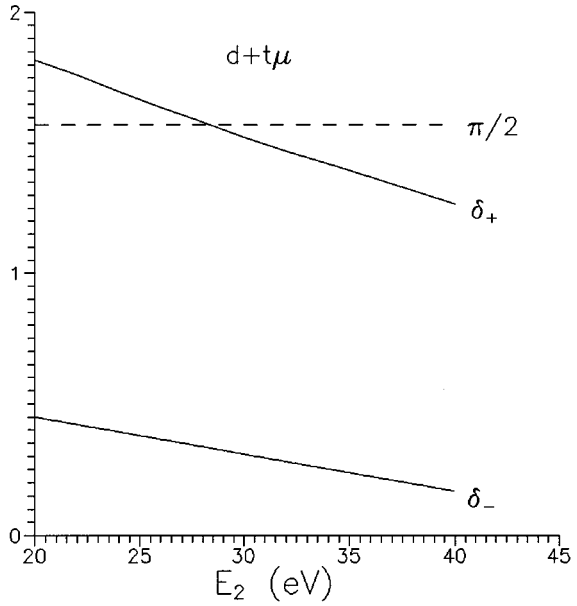

FIG. 12. Eigenphase shifts (55) of the S matrix for $d+t\mu$ scattering. The point $\delta_+=\pi/2$ is that of the fusion-in-flight peak in Fig. 11. The energy E_2 is measured with respect to the $d\mu(n=1)$ threshold.

a NSF Grant No. PHY-9013072 and by an allocation of computer time by the San Diego Supercomputer Center.

APPENDIX: HYPERFINE TRANSFORMATIONS

In this appendix we describe the relation between two different representations of the $J=0$ scattering states of a symmetric muonic atomic system $a+a\mu$. The first one is that where the spin s_{12} of the pair of nuclei is fixed, so that the states are classified by the parity $\wp=(-1)^{s_{12}}$ with respect to interchange of the nuclei. If the hyperfine interaction between nuclei and muon is neglected, the parity is an exact quantum number and this representation is very convenient, for it diagonalizes the three-body Hamiltonian (and the Faddeev equations). The second representation classifies the states by the spin s_{23} of the target muonic atom, so that there are two spin channels (25).

In the second representation, transitions between the spin channels (25) at fixed total three-body spin S are described by a symmetric reactance matrix $K^{(S)}=\{K_{ij}^{(S)}\}_{i,j=1,2}$. Corresponding s-wave cross sections for the transitions $i\to j$ are given by

$$\sigma_{ij}^{(S)}=\frac{4\pi a_\mu^2}{k_1^2}\,\frac{\delta_{ij}D_S^2+(K_{ij}^{(S)})^2}{(D_S-1)^2+T_S^2}, \tag{A1}$$

where the momentum k_1 is defined in (30),

$$D_S=\det\mathbf{K}^{(S)} \tag{A2a}$$

and

$$T_S=\mathrm{tr}\mathbf{K}^{(S)}. \tag{A2b}$$

Some simple spin algebra leads to the following expressions for the reactance matrices in terms of the fixed-parity phase shifts $\delta_\pm$:

$$\begin{pmatrix} K_{11}^{(S)} & K_{12}^{(S)} \\ K_{21}^{(S)} & K_{22}^{(S)} \end{pmatrix}=\mathbf{U}^{(S)}\begin{pmatrix} K_+ & 0 \\ 0 & K_- \end{pmatrix}[\mathbf{U}^{(S)}]^\dagger, \tag{A3}$$

where $K_\pm=\tan\delta_\pm$. The transformation matrices are (i) for $p+p\mu$ and $t+t\mu$,

$$\mathbf{U}^{(1/2)}=\frac{1}{2}\begin{pmatrix} 1 & -\sqrt{3} \\ \sqrt{3} & 1 \end{pmatrix}, \tag{A4a}$$

$$\mathbf{U}^{(3/2)}=\begin{pmatrix} 0 & 0 \\ 0 & -1 \end{pmatrix}, \tag{A4b}$$

and (ii) for $d+d\mu$,

$$\mathbf{U}^{(1/2)}=\frac{1}{\sqrt{3}}\begin{pmatrix} 1 & -\sqrt{2} \\ \sqrt{2} & 1 \end{pmatrix}, \tag{A5a}$$

$$\mathbf{U}^{(3/2)}=\frac{1}{\sqrt{6}}\begin{pmatrix} \sqrt{5} & -1 \\ -1 & -\sqrt{5} \end{pmatrix}, \tag{A5b}$$

$$\mathbf{U}^{(5/2)}=\begin{pmatrix} 0 & 0 \\ 1 & 0 \end{pmatrix}. \tag{A5c}$$

The above $\mathbf{U}$ matrices apply to even J (including s waves calculated in the present work); the $\mathbf{U}$ matrices for odd J are the same, *except* with the matrix columns interchanged.

Therefore, we have for $p+p\mu$ and $t+t\mu$,

$$\mathbf{K}^{(1/2)}=\frac{1}{4}\begin{pmatrix} K_++3K_- & \sqrt{3}(K_+-K_-) \\ \sqrt{3}(K_+-K_-) & 3K_++K_- \end{pmatrix}, \tag{A6a}$$

$$\mathbf{K}^{(3/2)}=\begin{pmatrix} 0 & 0 \\ 0 & K_- \end{pmatrix}, \tag{A6b}$$

and for $d+d\mu$,

$$\mathbf{K}^{(1/2)}=\frac{1}{3}\begin{pmatrix} K_++2K_- & \sqrt{2}(K_+-K_-) \\ \sqrt{2}(K_+-K_-) & 2K_++K_- \end{pmatrix}, \tag{A7a}$$

$$\mathbf{K}^{(3/2)}=\frac{1}{6}\begin{pmatrix} 5K_++K_- & \sqrt{5}(K_--K_+) \\ \sqrt{5}(K_--K_+) & K_++5K_- \end{pmatrix}, \tag{A7b}$$

$$\mathbf{K}^{(5/2)}=\begin{pmatrix} 0 & 0 \\ 0 & K_+ \end{pmatrix}. \tag{A7c}$$

Thereby, Eq. (58) implies

$$D_S=\det\mathbf{K}^{(S)}=K_+K_-, \tag{A8a}$$

$$T_S=\mathrm{tr}\mathbf{K}^{(S)}=K_++K_-, \tag{A8b}$$

and the formula (A1) for the cross sections is recast as

$$\sigma_{ij}^{(S)}=\frac{4\pi a_\mu^2}{k_1^2}[\,\delta_{ij}\sin^2\delta_+\sin^2\delta_-+(K_{ij}^{(S)})^2\cos^2\delta_+\cos^2\delta_-]. \tag{A9}$$

Substituting into this equation the above formulas for the K-matrix elements yields the following expressions for the cross sections in terms of the fixed parity cross sections $\sigma_\pm$, defined in (22), and the spin-flip cross section σ_{21} defined by (27): (i) for $p+p\mu$ and $t+t\mu$,

$$\sigma_{11}^{(1/2)}=\frac{1}{4}\sigma_++\frac{3}{4}\sigma_--3\sigma_{21}, \tag{A10a}$$

$$\sigma_{22}^{(1/2)}=\frac{3}{4}\sigma_++\frac{1}{4}\sigma_--3\sigma_{21}, \tag{A10b}$$

$$\sigma_{22}^{(3/2)}=\sigma_-, \tag{A10c}$$

$$\sigma_{12}^{(1/2)}=\sigma_{21}^{(1/2)}=3\sigma_{21}, \tag{A10d}$$

and (ii) for $d+d\mu$

$$\sigma_{11}^{(1/2)}=\frac{1}{3}\sigma_++\frac{2}{3}\sigma_--\frac{8}{3}\sigma_{21}, \tag{A11a}$$

$$\sigma_{11}^{(3/2)}=\frac{5}{6}\sigma_++\frac{1}{6}\sigma_--\frac{5}{3}\sigma_{21}, \tag{A11b}$$

$$\sigma_{22}^{(1/2)}=\frac{2}{3}\sigma_++\frac{1}{3}\sigma_--\frac{8}{3}\sigma_{21}, \tag{A11c}$$

$$\sigma_{22}^{(3/2)}=\frac{1}{6}\sigma_{+}+\frac{5}{6}\sigma_{-}-\frac{5}{3}\sigma_{21}, \tag{A11d}$$

$$\sigma_{22}^{(5/2)}=\sigma_{+}, \tag{A11e}$$

$$\sigma_{12}^{(1/2)}=\sigma_{21}^{(1/2)}=\frac{8}{3}\sigma_{21}, \tag{A11f}$$

$$\sigma_{12}^{(3/2)}=\sigma_{21}^{(3/2)}=\frac{5}{3}\sigma_{21}. \tag{A11g}$$

The spin-weighted effective cross sections (26) are (i) for $p+p\mu$ and $t+t\mu$,

$$\sigma_{11}=\sigma_{11}^{(1/2)}, \tag{A12a}$$

$$\sigma_{22}=\frac{1}{3}\sigma_{22}^{(1/2)}+\frac{2}{3}\sigma_{22}^{(3/2)}, \tag{A12b}$$

$$\sigma_{12}=3\sigma_{21}=\sigma_{12}^{(1/2)}, \tag{A12c}$$

and (ii) for $d+d\mu$,

$$\sigma_{11}=\frac{1}{3}\sigma_{11}^{(1/2)}+\frac{2}{3}\sigma_{11}^{(3/2)}, \tag{A13a}$$

$$\sigma_{22}=\frac{1}{6}\sigma_{22}^{(1/2)}+\frac{1}{3}\sigma_{22}^{(3/2)}+\frac{1}{2}\sigma_{22}^{(5/2)}, \tag{A13b}$$

$$\sigma_{12}=2\sigma_{21}=\frac{1}{3}\sigma_{12}^{(1/2)}+\frac{2}{3}\sigma_{12}^{(3/2)}. \tag{A13c}$$

Upon substituting in these equations the above formulas for $\sigma_{ij}^{(S)}$, we arrive at Eqs. (27).

[1] L. I. Ponomarev, Contemp. Phys. **31**, 219 (1991).
[2] W. H. Breunlich, P. Kammel, J. S. Cohen, and M. Leon, Annu. Rev. Nucl. Part. Sci. **39**, 311 (1989).
[3] L. Bracci *et al.*, Muon Catal. Fusion **5**, 21 (1991).
[4] S. I. Vinitsky and L. I. Ponomarev, Fiz. Elem. Chastits At. Yadra **13**, 1336 (1982) [Sov. J. Part. Nucl. **13**, 557 (1982)].
[5] L. Bracci *et al.*, Muon Catal. Fusion **4**, 247 (1989).
[6] C. Chiccoli *et al.*, Muon Catal. Fusion **7**, 87 (1992).
[7] J. S. Cohen and M. C. Struensee, Phys. Rev. A **43**, 3460 (1991).
[8] J. S. Cohen, Phys. Rev. A **43**, 4668 (1991).
[9] S. P. Merkuriev, Ann. Phys. (N.Y.) **130**, 395 (1980).
[10] A. A. Kvitsinsky, V. V. Kostrykin, and S. P. Merkuriev, Fiz. Elem. Chastits At. Yadra **21**, 1301 (1990) [Sov. J. Part. Nucl. **21**, 553 (1990)].
[11] A. A. Kvitsinsky and C.-Y. Hu, Phys. Rev. A **47**, 994 (1993); **47**, R3476 (1993); C.-Y. Hu and A. A. Kvitsinsky, Hyperfine Interact. **82**, 59 (1993).
[12] A. A. Kvitsinsky, A. Wu, and C.-Y. Hu, J. Phys. B **28**, 275 (1995); A. A. Kvitsinsky, J. Carbonell, and C. Gignoux, Phys. Rev. A **51**, 2997 (1995).
[13] L. D. Faddeev and S. P. Merkuriev, *Quantum Scattering Theory for Several Particle Systems* (Kluwer, Dordrecht, 1993).
[14] L. D. Faddeev, Tr. Mat. Inst. Akad. Nauk SSSR **69** (1963).
[15] A. A. Kvitsinsky, J. Carbonell, and C. Gignoux, Phys. Rev. A **46**, 1310 (1992).
[16] Ya. B. Zel'dovich and S. S. Gershtein, Usp. Fiz. Nauk **71**, 581 (1960) [Sov. Phys. Usp. **3**, 593 (1961)].
[17] Y. Kino and M. Kamimura (unpublished).
[18] Y. Kino and M. Kamimura, Hyperfine Interact. **82**, 45 (1993).
[19] K. Langanke and D. Lukas, Few-Body Syst. **13**, 87 (1992).
[20] V. S. Melezhik, Nucl. Phys. A **550**, 223 (1992).
[21] L. N. Bogdanova, V. E. Markushin, V. S. Melezhik, and L. I. Ponomarev, Yad. Fiz. **34**, 1191 (1981) [Sov. J. Nucl. Phys. **34**, 662 (1981)].
[22] W. A. Fowler, G. R. Caughlan, and B. A. Zimmerman, Annu. Rev. Astron. Astrophys. **5**, 525 (1967).
[23] V. I. Serov, S. N. Abramovich, and L. A. Morkin, At. Energ. **42**, 59 (1977) [Sov. J. At. En. **42**, 66 (1977)].
[24] P. Froelich, A. Floeres-Riveros, J. Wallenius, and K. Szalewicz, Phys. Lett. A **189**, 307 (1994).
[25] C.-Y. Hu, A. A. Kvitsinsky, and J. S. Cohen, J. Phys. B **28**, 3629 (1995).
[26] J. S. Cohen, in *Review of Fundamental Processes and Applications of Atoms and Ions*, edited by C. D. Lin (World Scientific, Singapore, 1993), Chap. 2.
[27] D. Harley, B. Müeller, and J. Rafelski, Z. Phys. A **336**, 303 (1990).